UNIVERSITAT POLITÈCNICA DE VALÈNCIA

ETS INGENIEROS DE CAMINOS, CANALES Y PUERTOS

TRABAJO DE FIN DE MÁSTER

Evaluation and assessment of wind effects on Banafjäl bridge (Västernorrland, Sweden) during its construction.

Presentado por

Martínez López, Guillermo

Para la obtención del

Máster Universitario en Ingeniería de Caminos, Canales y Puertos

Curso: 2018/2019

Fecha: Junio 2019

Tutor: José Casanova Colón

Cotutor: Mahir Ülker-Kaustell

Abstract

Wind is dynamic by nature, but its actions on structures were considered as static loads until the collapse of Tacoma Narrows Bridge (1940). Nowadays, due to the developments in civil engineering, bridge designs are becoming slenderer and lighter, which makes wind dynamic effects even more important than wind static effects. Furthermore, some types of bridges show specially vulnerable situations during constructions stages, when the structure is lighter or does not have its final stiffness. The aim of this document is to assess the dynamic wind loading on simple girder bridges during their construction phases. Particularly, the studied section is formed by two steel beams supporting a concrete slab. The analysis was made when the concrete slab has not been built yet and only the steel parts are in their positions. Eurocode 1 proposes some analytical methods to analyse dynamic wind loads, but the parameters given are only for simple sections.

Several CFD simulations were done with the software Ansys-Fluent to find the aerodynamic parameters depending on section's dimensions. The geometrical parameters tested were the height of the beams (h), the distance between beams (d) and the height of the bridge (H). Three values were assigned to each parameter, and beams' width was set to $b = 0.9\,m$. Tree construction stages were analysed. First, when only one beam is exposed to the wind, second, when the two beams are in their final locations but they are not connected yet and, by last, when both beams are joined by the bracing. Extra fluid simulations were made with closed sections, in order to see if isolating the space between the beams with plates improves section's vulnerability. The results showed that vortex shedding effects are stronger in the along-wind direction due to the low horizontal bending stiffness of the beams and their high area perpendicular to the flow. Increasing beams' distance showed to be a good solution to reduce wind effects. However, the alternative of closing the section with light plates had the best results, decreasing the frequency of vortex shedding and its effects.

Moreover, the obtained results were used to analyse the vulnerability of Banafjäl Bridge with the methods proposed by Eurocode 1. The effects of vortex shedding on the bridge showed to be of importance only when just one beam is in its final location. The low actions seemed to be because of the low frequencies of the bridge, which caused the resonance to occur with low wind speeds. Increasing bridge's natural frequencies the wind loads would increase, leading to high accelerations that could reduce the safety or the comfort of the workers. Anyway, the stresses were far from steel's elastic limit. Regarding buffeting loads, with wind speeds above 25-30 m/s, or 40-45 m/s when the bracing is done, the elastic limit of the steel was reached, leading to undesirable residual stresses in the beams. Increasing beams' width was in this case the best option to reduce buffeting effects.

Keywords: Vortex shedding, Buffeting, Dynamic wind effects, Computational Fluid Dynamics, Parametric study, Simple girder bridge, Structure aerodynamics.

Preface

The present master thesis was made for the Department of Civil and Architectural Engineering in the Royal Institute of Technology (KTH), with the collaboration of Tyréns AB.

I would like to express my sincere gratitude to Prof. Raid Karoumi for his suggestions and continuous support during the realisation of this project. I also would like to thank him for giving me the opportunity to work in a really interesting topic, learning every day about a beautiful field of study.

My most sincere gratitude to Dr. Mahir Ülker-Kaustell for his guidance and ideas during the past months. A big part of this master thesis comes from my conversations with him. I would also like to give him my thanks for opening me the doors of Tyréns AB during this period.

I am thankful to Prof. Sasan Sadrizadeh for introducing me in the world of CFD and for his guidance with the fluid simulations. I would like to thank him and Prof. Stefan Wallin for their advice regarding the calibration and verification of the models.

I would like to express my gratitude to my parents, who always encouraged me to pursue my goals and allowed me to be here enjoying this academic experience. They are models to follow for me.

Finally, I would like to give a special thanks to Ana Pérez Torres for her continuous support and help with the report. I will never now if I would have ended this master thesis without her.

Stockholm, 19th July 2019
Guillermo Martínez López

Contents

Chapter 1

Introduction

1.1 Background

The consideration of wind effects has been present in the design of bridges since many years ago. Even though bridges do not offer a large area normal to the wind flow, they are structures highly exposed to their effects. They are usually built over rivers or deep valleys, where the wind climate is stronger than in urban areas, and their slenderness makes them specially sensible to the wind's loading.

Wind loads are dynamic by nature, multiple phenomenons in the flow produce variations in the pressures around the structure's section, which translates into variable forces. However, due to the complexity of the phenomenons involved, wind effects were considered as static loads during a long period of time.

In the mid years of the 19th century two bridge collapses caused by the wind were recorded: Angers Bridge in France (1850) and Wheeling Suspension Bridge in the United States (1854). The first one failed due to the combined dynamic effects of the wind and a battalion of soldiers crossing the bridge during a storm, while the second one collapsed due to the torsional and vertical oscillations caused by the wind. Nevertheless, it was not until the collapse of Tacoma Narrows Bridge (1940) when the dynamic effects on bridges started to be deeply investigated. The bridge showed, during more than an hour before breaking, high torsional and bending amplitudes with lower frequencies than the natural ones of the structure, a phenomenon that was later called *fluttering*.

Similar effects had been observed since the First World War in some aircraft elements like the wings. It was rapidly proved that, when the wind drive a structure into high displacements, the structure itself affects the flow behaviour, which also affects the structure. Thus, the study of the phenomenons involved should combine both fields of study: elasticity and aerodynamics. A new field of study called *aeroelasticity* was born, trying to assess the interaction of both fluid and solid during the vibrations of the structure.

Since then, the number of authors interested in the field has increased and the knowledge of the wind-structure interaction has improved rapidly. The research has been focussed always in finding ways to simplify and generalize the phenomenon, designing analytical methods to describe wind effects and finding the parameters involved. In other words, the efforts have been focussed in

the design of easy methods which can be implemented in codes and regulations, reducing the dependence on the physical models during the design procedure of a structure.

In the early sixties A. G. Davenport defined the turbulence in the wind with the help of statistical concepts [6], setting the basis for the evaluation of the along-wind response of structures. The research of Davenport was focused on characterizing the static and dynamic loads in the direction on the wind, studying the influence of the gusts on the structure [7, 8, 9]. These dynamic effects caused by the turbulence were called *buffeting*. Authors as E. Simiu [36, 37] soon followed his work in the seventies and eighties, trying to improve the analytical methods to define the loads in the wind's direction.

Regarding the across-wind response, it was observed that the main phenomenon involved was the Von Karman vortex street, which periodically changed the pressure distribution around the structure's section. The effects of vortex shedding were specially strong when its frequency matched the natural frequencies of the structure, causing large amplitudes of vibration. The principal developments in this area come from H. Ruscheweyh in Germany [32, 33] and B. J. Vickery and R. I. Basu in Canada [49, 47, 48]. However, the analytical models developed in each country are quite different [12].

Unfortunately, the behaviour of the wind is strongly dependent on the shape of the structure affected, and the variety of bridge cross-sections makes more difficult to design generalized analytical methods to simplify the problem. Most studies on the subject have been done on simple cross-sections like the circle. Thus, the main part of the knowledge has been applied to the analysis of high stacks, bridge piles, cables or other structures with circular cross-section. Only a few authors, among whom R. H. Scanlan can be highlighted, focused their research on bridges, studying more deeply aerodynamic instabilities as fluttering, more typical in flat cross-section structures such as suspension bridges and aircraft wings.

The complexity of the problem can be also observed in Eurocode 1 [14]. The normative provides a comprehensive definition of methods to calculate the static wind load but it only describes the dynamic problems in informative annexes. Furthermore, the methods proposed in Eurocode 1 to calculate the dynamic wind load have shown to be a bad approximation in some cases [12], proving that more research is needed to find accurate and reliable analytical methods to estimate the structure's response.

Therefore, the task of dynamic wind load evaluation on bridges can be quite complicated. On the one hand, there is not official accord regarding analytical methods developed to estimate the dynamic wind loads. On the other hand, most of the analytical methods use parameters depending on the shape of the structure. Thus, wind analysis are usually done with a combination of analytical models, full-scale measurements, wind-tunnel tests and numerical models [38, 39].

Nowadays the importance of the dynamic loads is increasing strongly. The developments in structural engineering are allowing the designers to make lighter and more efficient structures every year, which translates into slender and flexible shapes. Due to the vulnerability of these designs to dynamic loads, the number of recorded cases of vibrations in structures has increased in the last years. The Volgograd Bridge (2010) in Russia is probably one of the most known cases, after showing high across-wind vibrations one year after its inauguration.

Furthermore, some types of bridges show specially vulnerable situations during construction phases. The construction of the concrete parts of the structure is usually made after the construction of

the steel parts, which means that the structure is less stiff during its construction than in the final stage. Besides, at some stages of the procedure, the concrete is in its place but it is not hardened yet, adding all its mass to the structure but none of its stiffness.

Moreover, the fast improvement of numerical methods and computers' capabilities has extended the use of Computational Fluid Dynamics (CFD) in the field, increasing the possibilities in wind engineering research. CFD has two main advantages respect to physical modelling: its easiness to extract data from the simulations and its almost zero cost. However, the reliability of CFD is still very limited by the computational time. It is still needed to complement the numerical simulations with wind tunnel tests for calibration and validation [16].

In conclusion, the evaluation of the wind loads on bridges is not an easy task, specially the dynamic ones. The complexity and quantity of phenomenons involved makes very difficult to generalize their effects and develop good analytical methods to calculate them. Furthermore, the main part of the research has been focussed on simple shapes, leaving a lack of information regarding more complex geometries. Therefore, the evaluation of dynamic wind-induced loads is still carried out for each single case, and usually reserved to high and long suspension bridges, leaving the evaluation of the most simple cases to the analytical methods showed in the codes.

1.2 Aim and scope

The aim of this document is to make an assessment of the dynamic wind loading induced by vortex shedding in simple girder bridges during their construction phases. Particularly, the studied section is formed by two steel beams supporting a concrete slab. The analysis will be made when the concrete slab has not been built yet and only one or both beams are already in their positions.

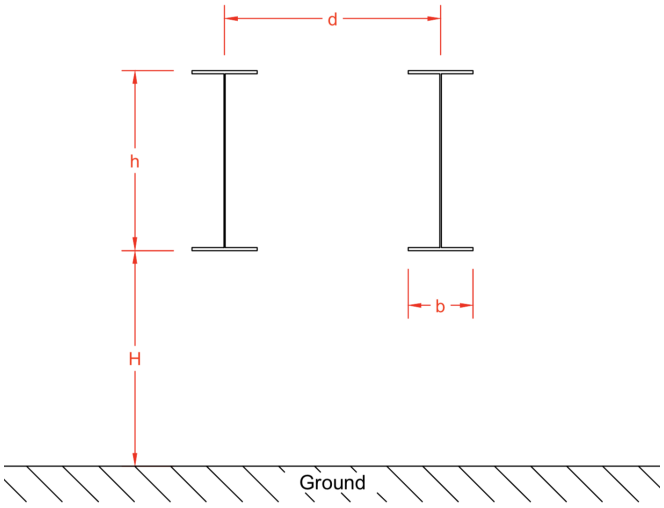

Figure 1.1: Section's sketch of the bridge before the construction of the slab, including the parameters of the geometry.

This type of bridges is widely used in Sweden and are specially vulnerable to dynamic loads before the construction of the slab. The long span, low weight and low stiffness of the steel beams make them specially susceptible to periodic wind loads, driving to the appearance of high stresses or even their overturn before the bridge is completed.

The study is focussed on the analysis of the frequencies and force coefficients generated by the alternative vortex shedding at both sides of the structure. Vortex shedding effects can be problematic with wind speeds around 5-15 m/s [16], while buffeting effects caused by wind turbulence are often dangerous for the structures with higher winds [12]. Assuming that the bridge is not going to stay without the concrete slab during a long period of time, the analysis of lower winds –but with a higher probability of occurrence– is considered more interesting for the evaluation in construction phases.

In order to make the assessment of the vortex shedding effects, several models will be made with the Computational Fluid Dynamic (CFD) software Ansys-Fluent, using RANS turbulence models. With them, several geometries will be tested extracting the Strouhal number and the drag and lift coefficient time series. The geometries tested include models with one and two beams, with the intention of evaluating the different situations during the construction of the bridge.

Unfortunately, making a proper validation with wind tunnel tests is out of scope of a master thesis due to the high complexity and work that is needed to test only a single geometry. Therefore, the CFD results can only be validated with literature data. Taking into account that the accuracy of RANS models is not very high in these problems [22], the study aims to make a qualitative assessment of the influence of each geometric parameter, rather than a quantitative analysis.

By last, the Banafjäl Bridge will be examined according to the results obtained in the previous tasks. The intention is to apply the research made in the parametric study to see its influence in the design procedure of a bridge.

1.3 Objectives

Accordingly with the aims described previously, the objectives of the report can be summarized as follows:

1. Describe the the wind characteristics and its behaviour around bluff-bodies, focussing in how the corresponding phenomena involved can create dynamic loads on the structure.

2. Describe the approach taken by Eurocode 1 to treat dynamic wind loads on structures, and more specifically on bridges. Describe also other approaches taken by other codes.

3. Explain how vortex shedding around bluff-bodies can be modelled and how the loads caused in the structure can be extracted, enumerating the different assumptions taken during the modelling procedure and assessing the reliability of the results.

4. Analyse the influence of the different geometry parameters showed in Figure 1.1 on the vortex shedding frequency and load intensity, showing the results in a graphical way that facilitates the subsequent design procedure of a bridge.

5. Propose some measures that can be taken to reduce the risk of incidents related to vortex shedding induced loads in the structure.

6. Make an assessment of the Banafjäl Bridge vulnerability to vortex shedding induced loads, proposing measures to improve its behaviour if necessary.

1.4 Limitations

Due to the limited time and resources available for the realisation of this master thesis, the report has certain limitations that need to be taken into account.

The first limitation, and the most important one, is the lack of wind tunnel tests or full-scale measurements for the validation of the numerical models. As said in section 1.1, the lack of accuracy when modelling wind's behaviour makes necessary to complement the simulations with physical measurements [39, 38], which was not possible for this project.

Unfortunately, the preparation of wind tunnel tests is out of scope for a master thesis project, due to the time and economical resources needed to carry it out. Therefore, the results from the numerical models needs to be treated carefully, focussing in the qualitative part instead of in the quantitative one.

On the other hand, the schedule for the project also limited the computational time of the numerical simulations. Using Direct Numerical Simulation (DNS) or Large Eddy Simulation (LES) as turbulence models leads to more realistic results compared to the ones using Raynolds-Averaged Navier-Stokes turbulence models [44]. Nevertheless, the usage of DNS or LES implies a longer time to validate the models as well as longer computational time during the simulations. Thus, it was considered that RANS modelling is more appropriate for the scope of this report, despite its limited accuracy.

Chapter 2

Wind loads on structures

2.1 The atmospheric boundary layer

The atmospheric boundary layer is the zone of the atmosphere where wind's behaviour is affected by the presence of the ground. Due to the viscosity of every fluid, the speed along a surface is zero, affecting the distribution of velocities in the vicinity. Meanwhile the flow normal to the surface is also zero, forcing the air to move parallel to the surface. Practically all civil engineering structures are inside this layer so, in order to fully understand how the wind affects a structure, it is important to understand the characteristics of the fluid in it. During the last century, a lot of effort has been devoted in finding good ways to define wind's behaviour within this layer.

Unfortunately, wind definition is not a simple problem. The chaotic behaviour of the air makes necessary to consider several events that affect the final speed and pressure fields of the fluid. These variations in the speed of the air can be seen in a wide range of spatial and temporal scales. From climate events lasting days and covering hundreds of square kilometres to the micro-scale turbulence in the molecules of the air.

Due to this difference in the scales of the mechanisms involved, wind speed can be defined mathematically as a addition of two terms: a mean wind speed depending on the wind climate and an random variable representing air's turbulence. Assuming that in the proximity of the floor there is no mean speed perpendicular to it, the three components of the wind can be mathematically described as [12]

$$\text{Longitudinal direction} \rightarrow U(z) + u(x, y, z, t) \tag{2.1}$$

$$\text{Transversal direction} \rightarrow v(x, y, z, t) \tag{2.2}$$

$$\text{Vertical direction} \rightarrow w(x, y, z, t) \tag{2.3}$$

where U is the mean wind speed and u, v and w the three components of turbulence.

However, the problem relies on where to put the border between wind climate and micro-scale turbulence. Studying this, van der Hoven built an autospectrum of the wind velocity based on measurements at 100 meters height and found that its value was lower between periods of 10 min

and 5-10 hours, denoting a clear distinction between wind climate events and turbulence [45]. Later, Courtney *et al.* built another autospectrum based on measurements at 30 meters height [4], upholding the existence of the mentioned spectral gap. In Figure 2.1 both autospectra can be observed.

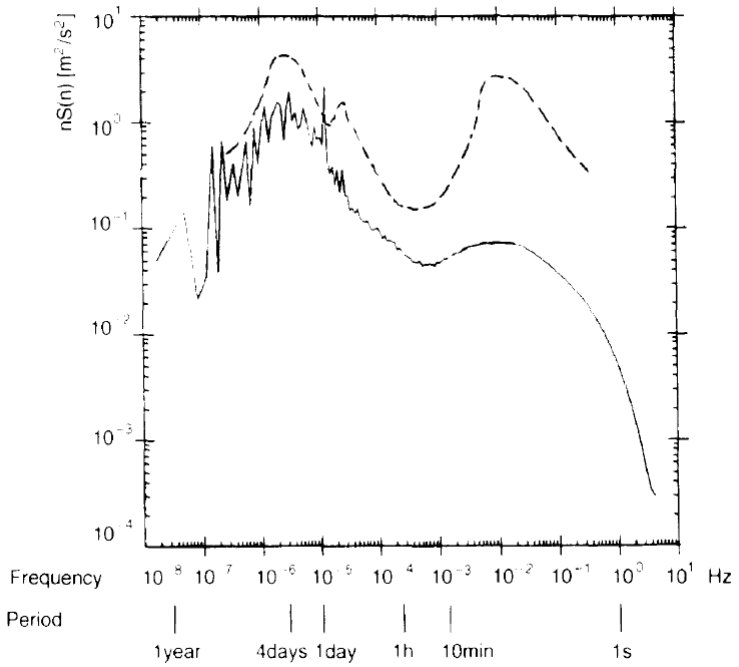

Figure 2.1: Wind power spectrum proposed by van der Hoven (dashed line) [45] and calculated by Courtney and Troen (continuous line) [4]. Source: *Wind loads on structures* [12].

In Eurocode 1 and in several other documents a time of 10 minutes is used to calculate the mean wind speed in equation 2.1, separating then wind climate effects and the turbulence. Both things can be treated then individually. On the one hand, the calculation of the mean wind speed, and on the other hand, turbulence definition.

2.1.1 Wind profile

In order to calculate the mean wind speed inside the atmospheric boundary layer it is necessary to determine how the ground affects the flow. As said before, the wind speed is zero at the ground and grows with height until the end of the boundary layer, but the relation between both terms is not linear.

Two formulas have been extensively used to determine the wind speed depending on the hight: the logarithmic profile and the power-law profile.

The logarithmic profile

The logarithmic profile has been widely used because its accuracy for moderate heights. Its expression to define the mean wind speed is

$$U(z) = u_* \frac{1}{k} \ln \frac{z}{z_0} \tag{2.4}$$

where k is von Kármán's constant (approximately 0.4), z_0 is the roughness length and u_* is the friction velocity. The last one can be defined as

$$u_* = \sqrt{\frac{\tau_0}{\rho}} \tag{2.5}$$

where ρ is the air density and τ_0 is the shear stress at the ground. The roughness length, principal parameter of the expression, can be defined as the height of the ground's roughness or, in other words, the size of the eddies formed by the protuberances in the surface (Figure 2.2). Eurocode 1 uses the logarithmic profile to define the mean wind speed and gives values for z_0 depending on the category of the terrain.

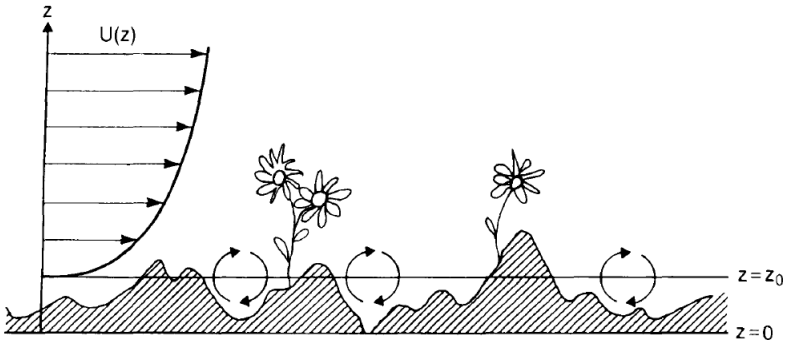

Figure 2.2: Basic representation of the roughness length [28].

It is important to say that for very high altitudes the logarithmic profile loses accuracy due to the increasing importance of the width of the boundary layer [12]. To overcome this problem R. I. Harris and D. M. Deaves proposed in 1980 a corrected logarithmic profile [11].

The power-law profile

Another expression used because of its simplicity is the power-law profile. The Canadian code NBC 1990 [27] uses this formula to determine mean wind speeds. Its expression can be written as

$$U(z) = U(z_{ref}) \left(\frac{z}{z_{ref}} \right)^{\alpha} \tag{2.6}$$

where z_{ref} is the reference height, $U(z_{ref})$ is the mean wind speed at the reference height and α is a parameter depending on the surface roughness.

2.1.2 Wind turbulence

The particles of a fluid are not tied to each other as it happens in a solid. Each particle follows its own path, defined by the interaction with the particles nearby. This behaviour, despite being technically possible to define, leads to a chaotic behaviour in the wind of such complexity that can only be approached with statistical methods. Therefore, the turbulence has always been defined as an stochastic process, with its random variables.

According to Dyrbye *et al.* [12], a normal distribution for the turbulence is an acceptable approximation for heights up to 100 or 200 metres. The turbulent component of the wind is the variation respect to the mean speed so it has, by definition, a zero mean. Thus, the statistical parameter needed to define it is the standard deviation.

Armitt proposed in 1976 that the turbulence is nearly constant for the lower half of the boundary layer [1], and he estimated the values of the standard deviation as

$$\sigma_u = Au_* \qquad \sigma_v \simeq 0.75\sigma_u \qquad \sigma_w \simeq 0.5\sigma_u \tag{2.7}$$

where A is a factor that depends on surface roughness and is aroun 2.5 for $z_0 = 0.05$ and around 1.8 for $z_0 = 0.3$. Having the standard deviations of the turbulence it is easy to calculate its intensity I_u in the along-wind direction:

$$I_u = \frac{\sigma_u}{U} \tag{2.8}$$

Time scales and integral length scales

Time scales and integral length scales represent the order of magnitude of the time and length sizes of the eddies in the wind. They are defined based on the autocorrelation and cross-correlation functions of the wind.

The autocorrelation function represents the similitude between a time series and the same time series delayed a time τ. Then, the larger are the eddies in the wind, the longer remains the autocorrelation function with high values. As wind's turbulence has a zero mean value, the autocorrelation function can be defined as the normalized mean value of the wind turbulence multiplied by the wind turbulence after a time τ. For the longitudinal component of the wind $\rho_u^T(z,\tau)$:

$$\rho_u^T(z,\tau) = \frac{E\{u(x,y,z,t)\cdot u(x,y,z,t+\tau)\}}{\sigma_u^2(z)} \tag{2.9}$$

In order to have a measure of correlation avoiding the use of the new variable τ, the concept of time scale was introduced. The time scale $T(z)$ is defined as

$$T(z) = \int_0^\infty \rho_u^T(z,\tau)d\tau \tag{2.10}$$

Note that the time scale will be high if the frequency of the turbulence is low, and the same in the opposite way. Furthermore, as the analysis is made in the boundary layer, it can be assumed that the time scale only varies with height.

Moreover, the integral length scale can be defined similarly from the concept of cross-correlation. The cross-correlation compares the time series between two different points at a distance r. In the principal direction of the wind, the cross-correlation $\rho_u^x(z, r_x)$ can be defined as

$$\rho_u^x(z, r_x) = \frac{E\{u(x, y, z, t) \cdot u(x + r_x, y, z, t)\}}{\sigma_u^2(z)} \tag{2.11}$$

While the integral length scale $L_u^x(z)$ is

$$L_u^x(z) = \int_0^\infty \rho_u^x(z, r_x) dr_x \tag{2.12}$$

It is important to mention that there are three time scales and nine integral length scales, depending on the component of the turbulence and the direction of the distance r taken.

In 1975, Counihan proposed empirical expressions to calculate the integral length scales depending on the height and the surface roughness [3]. His formulas are a good approximation for heights between 10 and 240 metres, being useful for most civil engineering purposes. The expresions proposed by Counihan are

$$L_u^x(z) = Cz^m \qquad L_u^y(z) \simeq 0.3 L_u^x(z) \qquad L_u^z(z) \simeq 0.2 L_u^x(z) \tag{2.13}$$

where C and m are parameters depending on the surface roughness and can be extracted from Figure 2.3.

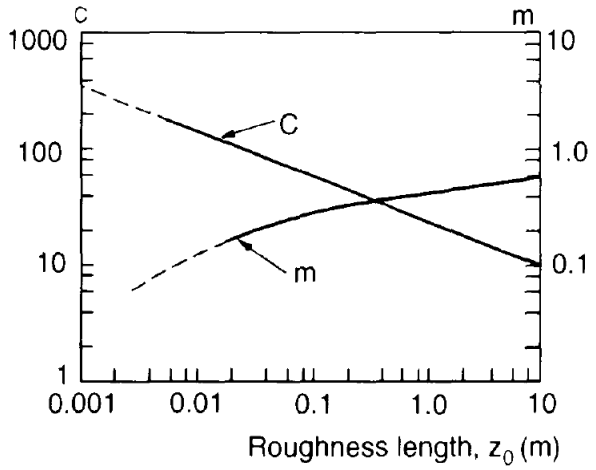

Figure 2.3: C and m parameters depending on the roughness length [3].

Power-spectral density functions

The power-spectral density function states the amount of energy contained in a certain band of frequencies. Defining it, it is possible to know which frequencies predominate in wind's turbulence and are dangerous for a structure. The normalised power-spectral density function is:

$$R_N(z,n) = \frac{nS_u(z,n)}{\sigma_u^2(z)} \tag{2.14}$$

where $S_u(z,n)$ is the power spectrum and n is the frequency. On the other hand, the frequency also needs to be normalised by the following expression:

$$f_L = \frac{nL_u^x(z)}{U(z)} \tag{2.15}$$

The energy of turbulence is generated by large eddies and dissipated in small eddies. Nevertheless, for a wide range of frequencies in between the energy stays constant [12]. This range is called the inertial subrange, and the non-dimensional power spectrum can defined there as

$$R_N(z,n) = Af_L^{-2/3} \tag{2.16}$$

where A is a parameter based in full-scale measurements. In ESDU 85020 a value of $A = 0.14$ is proposed for heights up to 200-300 metres [13]. However, it is important to mention that equation 2.16 is only valid for the inertial subrange, and overestimates the power spectrum for frequencies below 0.2 [38].

During the last century, several empirical expressions have been developed to define a normalised power-spectral density function which can be used in analytical methods, approximating also the values outside the inertial subrange. Von Kármán [51] proposed in 1948 the following expression, which slightly underestimates the values obtained with equation 2.16 for high frequencies:

$$R_N(z,n) = \frac{4f_L}{\left(1+70.8f_L^2\right)^{5/6}} \tag{2.17}$$

Davenport [8] proposed in 1967 another expression (equation 2.18) which overestimated the values in the inertial subrange and Harris [18] made a variation (equation 2.19) three years later to adjust the spectrum to a value of $A = 0.14$ in equation 2.16. Both formulas are valid for a specific integral length scale. In the case of Davenport $L_u^x \simeq 1200\,m$, while in Harris' equation $L_u^x \simeq 1800\,m$.

$$R_N(z,n) = \frac{2}{3}\frac{f_L^2}{\left(1+f_L^2\right)^{4/3}} \tag{2.18}$$

$$R_N(z,n) = \frac{2}{3}\frac{f_L}{\left(1+f_L^2\right)^{5/6}} \tag{2.19}$$

By last, Kaimal *et al.* [20] proposed in 1972 the following normalised power-spectral density function, which is now used by Eurocode 1:

$$R_N(z,n) = \frac{6.8f_L}{\left(1+10.2f_L\right)^{5/3}} \tag{2.20}$$

In figure 2.4 the previous power-spectral density functions are compared. Note that the proposed equations differ for very low frequencies. However, such low frequencies are not of importance when it comes to analysing wind effects on structures [12].

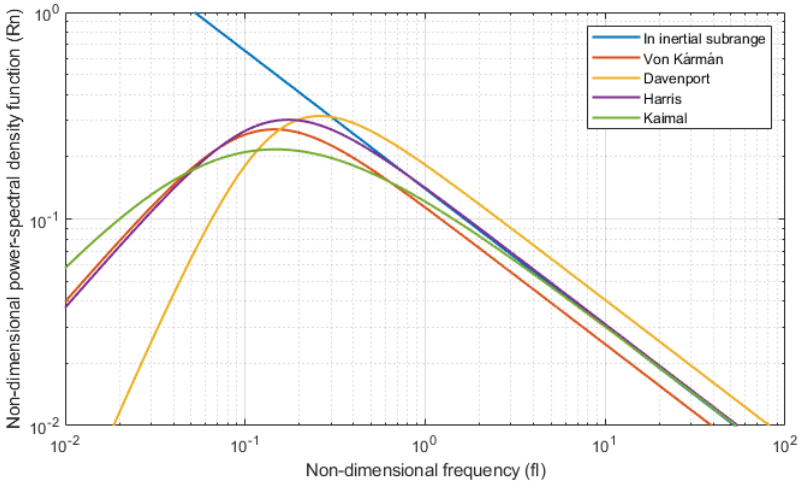

Figure 2.4: Normalised power-spectral density functions. For Davenport (2.18) and Harris (2.19) an integral length scale $L_u^x \simeq 180\,m$.

Correlation of the turbulence for particular pairs of points

In 1962, Davenport proposed an empirical formula to calculate the correlation of the turbulence between two particular points [7]. The proposed co-spectrum is

$$\psi(r,n) = exp\left(-\frac{n}{U}Cr\right) \tag{2.21}$$

where r is the distance between the points and C is the so-called *decay constant*, which needs to be obtained from full-scale measurements. Some years later, due to the anisotropic properties of the decay constant, Davenport [5] extended the definition to

$$\psi(r_y,r_z,n) = exp\left(-\frac{n}{U}\sqrt{(C_y r_y)^2 + (C_z r_z)^2}\right) \tag{2.22}$$

2.2 Bluff-body aerodynamics

As in the case of the ground for the atmosphere, any body immersed in a flow creates around it a boundary layer. In it, wind speed evolves from zero at the surface to the irrotational flow solution value. The dynamics of this boundary layer directly affect the final resulting forces on the body, and also creates unsteady effects as the vortex shedding.

In bodies with sharp edges or curves with very low radius the boundary layer suffers a detachment from the surface. Such type of shapes, more likely to create the mentioned detachment, are called *bluff-bodies*. The flow around them differs in behaviour from other streamline bodies such as airfoils. After the so-called *separation point* a recirculation zone is created to fill the space left by the boundary layer, resulting in the appearance of a vortex and a zone of low pressure in the vicinity of the shape.

2.2.1 Fluid induced forces

At every point of the surface of a body immersed in a fluid, the pressure of the fluid is acting against the body. The integration of this pressure over the contour of the body results in a force acting on the solid. In some cases, static situations for example, this integral results in zero resultant force. Nevertheless, when the flow is moving around the immersed shape there is usually a difference in the pressures before and after the body, resulting in a non-zero resultant force on the body.

In 2D cases, the resultant actions on the obstacle are usually divided in a drag force F_D in the direction of the flow, a lift force F_L perpendicular to the flow and a moment M. However, at the moment of analysing the behaviour of the flow around different shapes it is necessary to use dimensionless parameters, independent of the size of the body. Thus, in the literature the authors are usually referred to the drag coefficient C_D, the lift coefficient C_L and the moment coefficient C_M, defined as

$$C_D = \frac{F_D}{\frac{1}{2}\rho U^2 D} \tag{2.23}$$

$$C_L = \frac{F_L}{\frac{1}{2}\rho U^2 D} \tag{2.24}$$

$$C_M = \frac{M}{\frac{1}{2}\rho U^2 D^2} \tag{2.25}$$

where ρ is the density of the fluid, U is the oncoming wind speed and D is a representative length of the body, usually its dimension in the perpendicular direction to the flow.

2.2.2 The separation point

Inside the boundary layer, the flow needs to fulfil the next equation [21]:

$$u\frac{\partial u}{\partial x} + v\frac{\partial u}{\partial y} = -\frac{1}{\rho}\frac{\partial p}{\partial x} + \nu\frac{\partial^2 u}{\partial y^2} \tag{2.26}$$

where u and v are the components of the flow speed in the direction of the surface (x) and perpendicular to it (y) respectively, p is the pressure, ρ is the density and ν the kinematic viscosity of the fluid. Particularizing equation 2.26 for the surface the following expression is obtained:

$$\mu\frac{\partial^2 u}{\partial y^2} = \frac{\partial p}{\partial x} \tag{2.27}$$

where μ is the viscosity of the fluid. It is easy to deduce then that, if one side of the equation is negative, the other side will also be negative. Thus, when finding negative pressure gradients the curvature of the speed profile in the boundary layer changes.

In the case of a flow around a body, the streamlines deviate to surround the shape increasing the speed at both sides of the obstacle. By Bernoulli's equation it is known that a higher speed entails a lower pressure, so a negative pressure gradient will be found in the upstream zone of the body and a positive one will be found downstream, where the streamlines tend to separate again.

Therefore, applying equation 2.27, a negative curvature of the wind speed profile will be found at the upstream part of the obstacle, and a positive one will be found at the downstream side.

Taking into account that wind speed is zero on the surface and positive at the end of the boundary layer, a negative curvature of the wind profile will presumably imply a positive gradient in the surface and a positive speed at any point. Nevertheless, a positive curvature could mean positive or negative gradient at the surface, being possible to have negative speeds within the boundary layer.

The point where the gradient of the wind profile is zero at the surface is called *separation point*. Downstream of this point a reverse flow can be found, causing the separation of the upstream streamlines.

A summary of all the mentioned cases is shown in Figure 2.5. In the zone with negative curvature the gradient in the surface will always be positive, while in the zone with positive curvature, three different cases can be found.

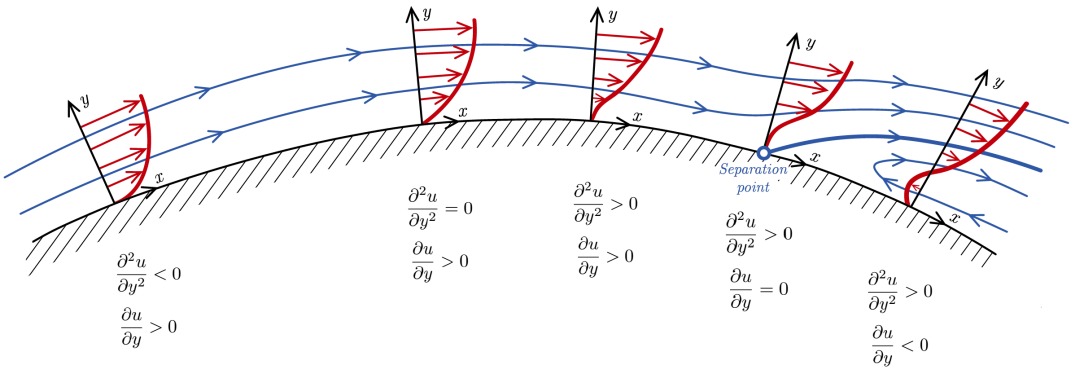

Figure 2.5: Different steps in the separation of the boundary layer.

Whether the positive pressure gradient is enough to cause the separation point or not is highly dependent on the shape of the obstacle [21]. Curved bodies can have the separation point in different locations depending on the Reynolds number. Turbulent boundary layers are less sensible to the pressure gradients so the detachment of the boundary layer will be found later in the surface. However, bodies with sharp edges will always have separation points in in the corners.

2.2.3 Low pressure zones

In the irrotational flow solution of the flow around a shape, there is no boundary layer and no separation point. Then, for symmetrical shapes, the pressure before and after the obstacle are equal and the resulting force on the body is zero.

Nevertheless, in real flows, after the separation point the backwards flow along the surface generates a vortex in the area near to the obstacle, creating a re-circulation zone. This zone is characterized by having very low pressures, generating a suction force on the body [38].

These zones create a difference between the pressure before and after the body, resulting in a

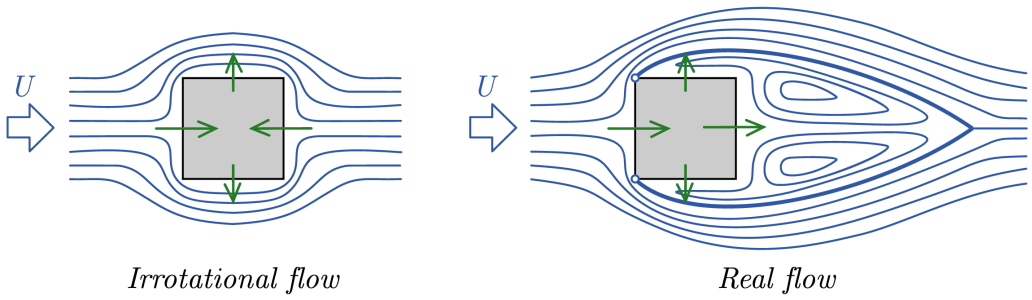

Figure 2.6: Streamlines for the flow solution in the case of irrotational flow (left) and in reality (right). Note that the separation point creates suction zones, increasing the drag coefficient.

positive drag force (Figure 2.6). Thus, the boundary layer behaviour has a great impact in the resulting aerodynamic properties of an object. Changing the separation point location can strongly affect the forces induced in an obstacle.

2.2.4 The von Kármán vortex street

As said before, depending on the Reynolds number the location of the separation point and the behaviour of the flow changes. With very low Reynolds numbers the viscous forces dominate the fluid and there is no separation point around the body, whereas slightly increasing Reynolds number the separation point appears with two stable vortexes of recirculation at each side of the shape [38]. By last, if Reynolds number is increased again, there is a moment where both vortexes become unstable and the process of vortex shedding starts, creating a chaotic wake downstream the obstacle. This last situation is called the *von Kármán vortex street*, named after the Hungarian scientific Theodore von Kármán, and is the main causative of periodic cross-wind loads in structures. All three cases are showed in Figure 2.7.

Despite all three stages are possible in any bluff-body, most civil engineering structures offer flow situations with Reynolds numbers around 10^5 or 10^6, clearly in the zone where the bluff-body is creating a wake. With such high Reynolds numbers the flow becomes turbulent and the phenomenon is difficult to see. However, the vortex shedding continues and so does the induced periodic forces.

The shape of the mentioned wake has a great impact in the aerodynamic properties of bluff-bodies, affecting the drag coefficient and the non-dimensional vortex shedding frequency, the so-called *Strouhal number*.

The Strouhal number

In 1878, Vincenc Stouhal observed that the frequency of the vortex shedding was proportional to the wind speed for a wide range of Reynolds numbers [42]. As the frequency was also inversely proportional to the obstacle's width, Strouhal proposed a dimensionless coefficient St to characterize the vortex shedding frequency:

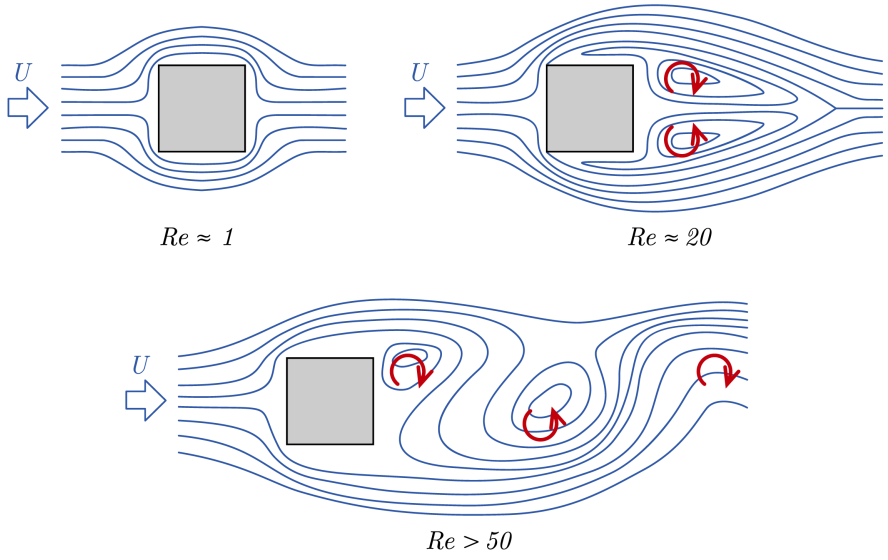

Figure 2.7: Different behaviours of the fluid past a square depending on the Reynolds number.

$$St = \frac{fD}{U} \tag{2.28}$$

where f is the frequency of vortex shedding. As Roshko observed in 1954 [30], this parameter showed to be highly dependent on the body's shape, being very useful to relate frequency and flow speed for given bodies. However, for a specific shape, the coefficient can be considered constant for a wide range of Reynolds numbers.

2.2.5 Wake influence

Experiments from Roshko [30] showed that the wake has a great influence in the drag coefficient and the Strouhal number, confirming the shape dependency of both parameters. Roshko proposed a variation of the Strouhal number based on the wake width and speeds, and reached similar values for it in experiments with several body shapes.

Applying the original definition of the Strouhal number (equation 2.28), as wider is the wake generated by the obstacle, smaller will be the width of the solid in proportion, and lower will be the Strouhal number. In the case of the drag coefficient a similar approach can be taken. The thinner is the wake generated by the body, the more aerodynamic it will be, resulting in a lower drag coefficient.

Unfortunately, in most cases the width of the wake is not only dependent on the shape of the body. The location of the separation point determines the angle of separation of the boundary layer, affecting the wake shape. For shapes with rounded edges the separation point is highly depending on the Reynolds number. When the boundary layer becomes turbulent, the flow remains more time attached to the surface and the separation point moves backwards. The moment when the

boundary layer becomes turbulent depends also in the surface's roughness. As rougher the surface is, sooner will be the transition.

The movement of the separation point usually creates a decrease in the wake's width, which is translated into a drop in the drag coefficient and sudden increase in the Strouhal number. However, for shapes with sharp edges, the separation point will always be located in the corner. Thus, bodies with sharp edges are usually considered Reynolds-independent [38].

2.3 Along-wind effects on structures

In the direction of the wind several types of forces are acting at the same time. On the one hand, there is an static load created by the mean wind speed and the low frequency turbulence, generating static deflections in the structure. On the other hand, the turbulence of the wind at frequencies near to the natural frequency of the structure may cause vibrations and a dynamic amplification. This last effect is called *buffeting*. Several parameters are involved in both dynamic and static loads, making the creation of analytical methods difficult.

It was not until the early sixties, when Davenport introduced a method to calculate maximum loads in the along-wind response [7]. In it, the maximum wind load can be calculated multiplying the mean wind load by a coefficient called the *gust factor*. Despite the method was initially used to calculate static wind loads, the dynamic movement of the structure can be easily included in the formulation, as it will be explained in section 2.3.2. For these cases, the term *equivalent static load* has been used among the field to describe a static load with the same effects for the structure than the static and dynamic loads together.

2.3.1 Davenport's model

The total wind load in the direction of the flow can be expressed as

$$F_{tot}(t) = C_D \frac{1}{2} \rho A U_{tot}^2(t) \tag{2.29}$$

where C_D is the drag coefficient, A is the area of the structure perpendicular to the flow, ρ is the fluid's density and $U_{tot}(t)$ is the total wind speed at a moment t. Applying expression 2.1, if the speed of the structure is not significant the last term of the previous equation can be expressed as

$$U_{tot}^2(t) = \big(U + u(t)\big)^2 \tag{2.30}$$

where U is the mean wind speed and $u(t)$ is the turbulence component. Assuming that the turbulence component is much smaller than the mean wind speed, the term $u^2(x)$ can be neglected, being possible to redefine equation 2.30:

$$U_{tot}^2(t) = U^2 + 2Uu(t) \tag{2.31}$$

The total force F_{tot} can be divided then into two terms: a force time-independent F_q representing the mean wind load and a fluctuating force $F_t(t)$ caused by the turbulence.

$$F_{tot}(t) = F_q + F_t(t) \tag{2.32}$$

$$F_q = C_D \frac{1}{2} \rho A U^2 \tag{2.33}$$

$$F_t(t) = C_D \frac{1}{2} \rho A U u(t) \tag{2.34}$$

Therefore, in order to calculate the maximum wind force, it is necessary to add the maximum value of the turbulence load to the mean wind load. Davenport proposed the following equation to calculate the maximum wind load:

$$F_{max} = F_q + k_p \sigma_F \tag{2.35}$$

where σ_F is the standard deviation of the wind load and k_p is the peak factor. The gust factor can be calculated then as

$$\varphi = \frac{F_{max}}{F_q} = 1 + k_p \frac{\sigma_F}{F_q} \tag{2.36}$$

It can be easily deduced from the integration of the power-spectral density function that σ_F / F_q is equal to two times the turbulence intensity, leaving the previous equation as

$$\varphi = 1 + k_p 2 I_u \sqrt{k_b} \tag{2.37}$$

where I_u is the turbulence intensity and k_b is the background turbulence factor, which introduces in the equation the influence of the correlation of the turbulence along the structure's surface. With big structures the loads induced by the turbulent component of the wind may not be synchronized, so k_b is equal to 1 in point-like structures and decreases as the exposed area increases. The background turbulence factor is calculated in line-like structures as

$$k_b = \int_0^\infty \chi^2 \left(\frac{nl}{U} \right) \frac{S_u(n)}{\sigma_u} dn \tag{2.38}$$

where $S_u(n)$ is the power-spectral density function of the wind, n is the frequency of the turbulence and χ^2 is the aerodynamic admittance function. The last one represents the correlation between the turbulence along the structure. For line-like structures it can be calculated as

$$\chi^2 \left(\frac{nl}{U} \right) = \frac{1}{l} \int_0^l 2 \left(1 - \frac{r}{l} \right) \psi_p(r, n, U) dr \tag{2.39}$$

where l is the length of the structure,r is the distance between two points on it and $\psi_p(r, n, U)$ is the correlation in the along-wind turbulence between both points, as defined in equation 2.22.

Regarding the peak factor, it is defined as the ratio between the maximum value of the turbulence component and its standard deviation. It can be calculated as

$$k_p = \sqrt{2 \ln(\nu T)} + \frac{\gamma}{\sqrt{2 \ln(\nu T)}} \tag{2.40}$$

where $\gamma = 0.577$ is Euler's constant, T is the period of time considered, usually equal to 600 seconds, and ν is the zero-upcrossing frequency. The last one is calculated as

$$\nu = \sqrt{\frac{n_0^2 k_b + n_e^2 k_r}{k_b + k_r}} \tag{2.41}$$

$$n_0 = \sqrt{\frac{\int_0^\infty n^2 \chi^2 \left(\frac{nl}{U}\right) S_u(n) dn}{\int_0^\infty \chi^2 \left(\frac{nl}{U}\right) S_u(n) dn}} \tag{2.42}$$

where n_0 is the representative frequency of the gust loading in a rigid structure and n_e is the frequency of resonance in the first horizontal mode of vibration.

2.3.2 Response of Single Degree of Freedom Systems

The general equation of a Single Degree of Freedom System (SDOF) is

$$m\ddot{\xi}_{def}(t) + c_s\dot{\xi}_{def}(t) + k\xi_{def}(t) = F_{tot}(t) \tag{2.43}$$

where ξ_{def} is the deflection, m is the mass of the system, c_s the damping and k the stiffness. In this case, the movement of the structure affects also the wind speed:

$$U_{tot}^2(t) = \left(U + u(t) - \dot{\xi}(t)\right)^2 = U^2 + 2Uu(t) + 2U\dot{\xi}(t) \tag{2.44}$$

Therefore, the total force F_{tot} will have a new component, caused by the aerodynamic damping:

$$F_{tot}(t) = F_q + F_t(t) - F_a(t) \tag{2.45}$$

$$F_a(t) = C_D \frac{1}{2} \rho A U \dot{\xi}(t) = c_a \dot{\xi}(t) \tag{2.46}$$

Moving F_a to the other side of the expression, equation 2.43 can be expressed as

$$m\ddot{\xi}(t) + (c_s + c_a)\dot{\xi}(t) + k\xi(t) = F_q + F_t(t) \tag{2.47}$$

Showing that the damping is formed by two terms: the structural damping c_s and the aerodynamic damping c_a generated by the movement of the structure. The last one has a critical role in the stability of the system since it also can have a negative value, as will be explained in section 2.5.

Regarding the gust factor, a new factor k_r is added to the expression of the coefficient to consider the increase of the load due to the resonance of the structure.

$$\varphi = 1 + k_p 2 I_u \sqrt{k_b + k_r} \tag{2.48}$$

The resonance factor k_r is zero when the dynamic effects are negligible, and is also dependent on the power-spectral density of the turbulence and the admittance function. However, note that in

this case only the value of the admittance function associated with the natural frequency of the structure n_e is needed.

$$k_r = \chi^2 \left(\frac{n_e l}{U} \right) \frac{n_e S_u(n_e)}{\sigma_u^2} \frac{\pi}{4\zeta} \tag{2.49}$$

where ζ is the damping ratio, defined as

$$\zeta = \frac{c_s + c_a}{2\sqrt{mk}} \tag{2.50}$$

Finally, it is important to mention that, for structures with linear behaviour, the gust factor can be directly applied to calculate the deflections from the mean deflection of the structure μ_ξ, which can be easily calculated from the mean wind load in equation 2.33.

$$\xi_{max} = \mu_\xi + k_p \sigma_\xi = \varphi \mu_\xi \tag{2.51}$$

$$\mu_\xi = \frac{F_q}{k} \tag{2.52}$$

2.3.3 Along-wind response in continuous structures

The maximum response of a structure with infinite degrees of freedom is also found adding the effects of the variation of the wind load to the mean response. The characteristic value of the response can be expressed as

$$R_{max} = \mu_R + k_p \sigma_R \tag{2.53}$$

$$R_{max} = \varphi \mu_R \tag{2.54}$$

where μ_R is the mean response and σ_R is its variance. However, in this case the peak factor will be slightly modified, introducing two new parameters, θ_b and θ_r, which introduce the effects of the influence functions in the structure.

$$\varphi = 1 + k_p 2 I_u \sqrt{\theta_b^2 k_b + \theta_r^2 k_r} \tag{2.55}$$

The peak factor k_p can still be calculated with equation 2.40, but the values of k_b and k_r can not be calculated with the same methods as in a SDOF. Therefore, the problem for continuous structures relies on finding the mean response of the structure μ_R and the parameters for the peak factor: θ_b, k_b, θ_r and k_r.

The mean response

In the case of bridges, the mean response is calculated integrating the mean wind load F_q, which depends only on z multiplied by a response-influence function I_r along the length of the bridge:

$$\mu_R = \int_0^l F_q(x) I_R(x) dx \tag{2.56}$$

$$F_q(x) = C_D(x) \frac{1}{2} \rho h(x) U^2(z) \tag{2.57}$$

where l is the length of the bridge, $h(x)$ is the height of its cross-section and $I_r(x)$ takes the value of the response generated by a unitary load applied in the position x. Note that the wind speed $U(z)$ depends only on z as explained in section 2.1.1. In the case of a bridge with constant section, the drag coefficient and the height of the section will remain constant, being possible to reformulate the previous equation as

$$\mu_R = C_D \frac{1}{2} \rho h U^2(z) \int_0^l I_R(x) dx \tag{2.58}$$

where the integral of $I_r(x)$ cab be easily calculated for any particular response of the bridge.

The gust factor

Particularizing the calculations of the gust factor for the case of an horizontal bridge with constant section and a mode shape with constant sign, the new parameters are directly calculated as

$$\theta_b = 1 \qquad \theta_r = \frac{\int_0^l \xi(x) dx \int_0^l \xi(x) I_R(x) dx}{\int_0^l \xi^2(x) dx \int_0^l I_R(x) dx} \tag{2.59}$$

where $\xi(x)$ is the first mode of vibration in the along-wind direction. However, for design purposes is possible to use $\theta_r = 1$ as well [12], leaving the definition of the gust factor as in equation 2.48. Regarding the background factor, it is calculated by the following expression:

$$k_b = \frac{\int_0^l \int_0^l \rho_u(r_x) I_r(x_1) I_r(x_2) dx_1 x_2}{\left(\int_0^l I_r(x) dx \right)^2} \tag{2.60}$$

where $\rho_u(r_x)$ is the correlation coefficient for longitudinal turbulence components. Dyrbye *et al.* [12] proposed in 1997 an easier expression (equation 2.61) based on values of the parameters usually found in real situations and substituting in equation 2.60.

$$k_b = \frac{1}{1 + \frac{3}{2} \sqrt{\left(\frac{b}{L_u} \right)^2 + \left(\frac{h}{L_u} \right)^2 + \left(\frac{3}{\pi} \frac{b}{L_u} \frac{h}{L_u} \right)^2}} \tag{2.61}$$

By last, for line-like structures the resonance factor is calculated by the following expression:

$$k_r = \frac{\pi^2}{2\delta} R_N(z, n_e) \frac{| J_x(n_e) |^2}{| J_z(0) |} \tag{2.62}$$

where δ is the damping expressed as the logarithmic decrement, $R_N(z, n_e)$ is the normalized power-spectral density function described in section 2.1.2 and $J_x(n)$ is the joint acceptance function in the direction of the bridge.

2.4 Cross-wind effects on structures

The principal contributor to the cross-loading of structures is the von Kármán vortex street. The cyclic vortex shedding changes periodically the velocity field of the fluid, which also changes periodically the pressure field around the body. During this cycle the speed at both sides of the obstacle changes alternatively depending on which vortex is being detached, creating a high difference of pressure in the direction perpendicular to the flow.

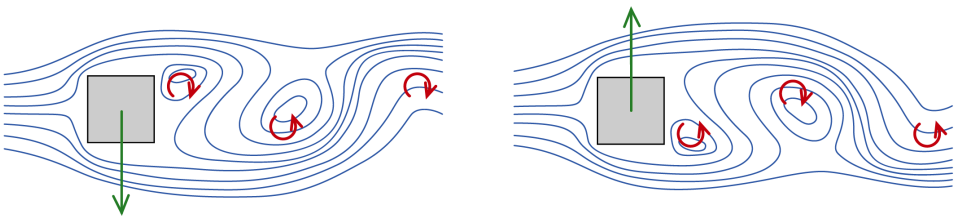

Figure 2.8: Variation of the lift force in two opposite moments of a vortex shedding cycle.

The result is the generation of a periodic lift force over the body (Figure 2.8, which can be approximated by a sinusoidal function [38]. Furthermore, it is important to say that the phenomenon also creates an oscillation in the along-wind direction, but with twice the frequency of the lift coefficient (Figure 2.9). The amplitude of the drag coefficient is usually much smaller than the one of the lift coefficient and its effects are usually neglected. However, for certain geometries with higher dimensions perpendicular to the wind the, drag force might need to be considered.

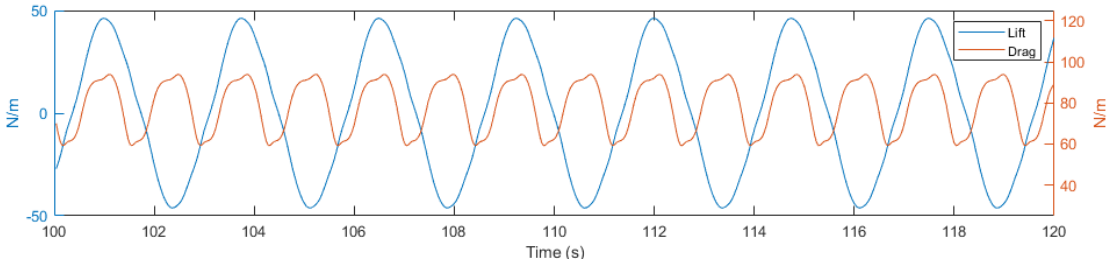

Figure 2.9: Drag and lift oscillations on a steel beam caused by vortex shedding. The results are extracted from CFD simulations.

Vortex shedding is usually dangerous when its frequency concur with the natural frequency of the structure, creating large amplitudes of vibration, while buffeting is more dangerous with high winds, when the turbulence component can create vibrations in the structure even though both frequencies are not equal. Thus, in general both phenomenons do not occur at the same time, making the evaluation of vortex shedding independent of buffeting phenomenon.

The range of wind speeds where vortex shedding is considered dangerous is 5-15 m/s [16]. For lower speeds the induced loads are not of importance, while with higher speeds the flow is considered governed by the turbulence and vortex shedding is chaotic, reducing the induced loads.

Besides the contribution of the vortex shedding, there are other phenomena involved in transversal loading. First, the turbulence in the direction perpendicular to the flow can also cause vibrations.

Second, the so-called *motion induced loads*. When the structure has large deformations the wind flow can be affected. The total force in the cross-wind direction can be defined then as

$$F = F_t + F_v + F_m \tag{2.63}$$

where F_t, F_v and F_m are the forces caused by the transversal turbulence, the vortex shedding and the motion of the structure respectively. However, the turbulence induced loads F_t is usually very low and can be neglected, except in the case of very tall bridges, were it can have an important influence in the overall effects [12]. In the case of an horizontal bridge, the vortex shedding load will have the following formula:

$$F_v(x,t) = q(x)h(x)C_L(x,t) \tag{2.64}$$

$$q(x) = \frac{1}{2}\rho U^2 \tag{2.65}$$

where $q(x)$ is the wind's velocity pressure, U is the mean wind speed at the height of the bridge, ρ is the density of the air, $h(x)$ is the vertical size of the deck and $C_L(x,t)$ is the lift coefficient, which will be oscillating because of the vortex shedding.

2.4.1 The influence of turbulence in vortex shedding

The turbulence of the wind also has an effect in the vortex shedding phenomenon. On the one hand, the variation of wind speed implies a variation in the vortex shedding frequency, which means that the frequency of the induced load will vary between a small range of frequencies. This effect can be described with a power-spectral density function, but in this case, the values will more concentrated than in of the along-wind turbulence power spectrum. Vickery *et al.* assumed a normal distribution of the turbulence and proposed the following normalized power spectrum [50], where the peak of the spectrum is located in the vortex shedding frequency:

$$\frac{nS_{C_L}(x,n)}{\overline{C}_L^2(x)} = \frac{n}{\sqrt{\pi}B(x)n_s(z)} exp\left[-\left[\frac{1-n/n_s(x)}{B(x)}\right]^2\right] \tag{2.66}$$

where $S_{C_L}(x,n)$ is the power spectrum of the lift coefficient, n is the frequency, $\overline{C}_L^2(x)$ is the variance of the lift coefficient, $n_s(x)$ is the vortex shedding frequency and $B(z)$ is the spectral bandwidth, which can be approximated as

$$B(z) = 0.1 + 2I_u \tag{2.67}$$

where I_u is the turbulence intensity in the along-wind direction, as stated in equation 2.8.

In the other hand, the vortex shedding usually is not in the same phase for all the length of the structure. The difference in phase has a favourable effect because the peak load is not founded at the same time in all the structure. This effect is usually considered considering a correlation length, where the loads are acting in the same phase. A reasonable approximation for this correlation

length for horizontal bridges –based in the coherence of the lift coefficient and its phase spectra– is [12]:

$$\frac{L'}{h} = \frac{\sqrt{\pi}}{2\sqrt{a}} exp\left(-\frac{b^2}{4a}\right) \tag{2.68}$$

where $a \sim 0.1$ and b are constants, being the last one dependent on the shape of the cross section.

2.4.2 Motion induced loads

The motion induced component of the cross-wind load is defined as

$$F_m = -h_a \ddot{\xi}_{def} - c_a \dot{\xi}_{def} \tag{2.69}$$

where h_a is the so-called *added mass of air*, c_a is the aerodynamic damping and ξ_{def} is the deflection of the structure. Introducing this term in the general equation of a SDOF, the following formula is obtained:

$$(m + h_a)\ddot{\xi}_{def}(t) + (c_s + c_a)\dot{\xi}_{def}(t) + k\xi_{def}(t) = F_t(t) + F_v(t) \tag{2.70}$$

where m is the mass of the system, c_s is the structural damping and k is the stiffness. The added mass of air is usually negligible, but the aerodynamic damping plays an important role in some cases. The aerodynamic damping can have negative values for frequencies slightly above the vortex shedding frequency, strongly amplifying the vibrations of the structure.

The aerodynamic damping is usually expressed with the dimensionless coefficient Sa:

$$Sa = \frac{2\delta_a m_e}{\rho h^2} \tag{2.71}$$

where δ_a is the logarithmic decrement of the aerodynamic damping and m_e is the modal mass divided by the length of the structure. In the same way, the structural damping can be expressed with the so-called *Scruton number*:

$$Sc = \frac{2\delta_s m_e}{\rho h^2} \tag{2.72}$$

where δ_s is the logarithmic decrement of the structural damping. Usually, the structure is safe with Scruton numbers above 20, and has a high risk of instability with Scruton numbers below 5. The large-scale turbulence influences also the risk of instability of the structure [12]. A high large-scale turbulence reduces the correlation of the vortex shedding and the phenomenon stays less time with steady frequency, while with low large-scale turbulence the vortex shedding will occur simultaneously along the structure, causing higher loads.

Lock-in

Several experiments state that the correlation length of the vortex shedding phenomenon increases with the motion of the structure [12]. This happens because large amplitudes of vibration affect wind's behaviour, forcing the vortex shedding to occur at the same frequency of the structure.

An interesting effect created because of this increase of correlation is the lock-in phenomenon. The synchronization of vortex shedding when the structure is in resonance creates even higher forces, creating larger amplitudes. When the structure is in this stage, the vortex shedding will be synchronized with the vibration frequency even if the wind speed increases, maintaining the resonance state (Figure 2.10).

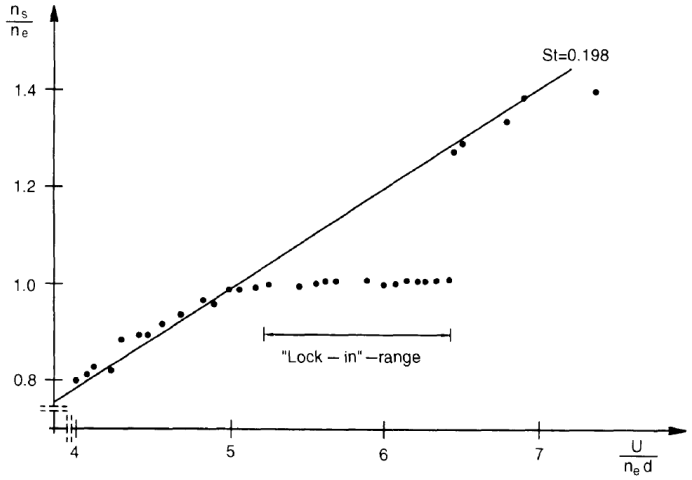

Figure 2.10: Experimental results of the frequency of vortex shedding in relation with the natural frequency of the structure for various wind speeds, showing the lock-in phenomenon. Source: Feng,1968 [15].

2.4.3 Vortex shedding response evaluation

The complexity of vortex shedding phenomenon has lead to the generation of very different analytical models to predict its effects [16]. Several codes around the world use very different methods with a considerable difference in its results. The main part of the methodologies proposed were though for particular type of cases, so it is necessary to understand the domain of application of each one to make a proper analysis of the cross-wind response of structures.

Probably, the most simple method is the sinusoidal method. In it, the load is assumed to be sinusoidal and acting always in the direction of the mode shape. Thus, for mode shapes with changing sign, the load direction will change sign depending on the location of the structure were the load is applied. The sinusoidal method does not consider the lack of correlation between the phases of the vortex shedding in different points, nor the changes in the mean wind speed. Therefore, the model leads to very conservative results. Basically, it calculates the worst case scenario, when the load is completely sinusoidal and acts in the most unfavourable direction.

In order to reach more realistic results, two different approaches have been taken. In the University of Western Ontario (UWO) the spectral model was developed. The method simulates the vortex

shedding loads with statistical methods, taking in to account that they will not be completely synchronized along the structure. This model gives accurate results for relatively stiff structures, such as concrete columns [12], but it is not focussed on modelling aeroelastic effects when the amplitudes of vibration are big.

A completely different approach was taken by Ruscheweyh in the Rheinisch Westfälische Technische Hochschule (RWTH) in Aachen, developing the vortex resonance model. Ruscheweyh takes into account the lack of correlation by defining an *effective correlation length* where the load is acting [31]. Therefore, the models simulates the synchronization of vortex shedding in the zones with larger amplitudes when the structure is in resonance, and assumes a single load in this area. The model has good results for flexible structures such as steel chimneys, where the amplitudes of vibrations force the flow to be synchronized in the correlation length [12].

The objective of this report is to analyse the dynamic behaviour of two slender steal beams when the concrete parts of the bridge have not been built yet. Therefore, the most appropriate method is the one proposed by Ruscheweyh. Considering the wide variety of approaches to define the effects of vortex shedding, only the mentioned method will be commented.

Vortex resonance model

The vortex resonance model directly calculates the maximum deflection of the structure, given by the following formula:

$$y_{max} = \frac{F_e}{(2\pi n_e)^2 m_e} \frac{\pi}{\delta_s} \tag{2.73}$$

where n_e is the natural frequency of the structure, m_e equivalent mass per unit length of the structure, δ_s is the logarithmic decrement of the structural damping and F_e is the equivalent load defined as

$$F_e = \xi_{max} \frac{\int_0^l q(x)h(x)c_F(x)\xi(x)dx}{\int_0^l \xi^2(x)dx} \tag{2.74}$$

where $q(x)$ is the correlation length, $h(x)$ is the transversal dimension of the bridge deck, $c_F(x)$ is a dimensionless factor describing the maximum value of the lift coefficient and $xi(x)$ is the first mode shape in the cross-wind direction. Particularizing for the case of an horizontal bridge with constant cross-section $q(x)$, $h(x)$ and $c_F(x)$ will be constant, so equation 2.73 can be rewritten as

$$y_{max} = \xi_{max} \frac{\int_0^l c_F(x)\xi(x)dx}{\int_0^l \xi^2(x)dx} \frac{q\,h}{4\pi n_e^2 m_e \delta_s} = \xi_{max} h \frac{\int_0^l c_F(x)\xi(x)dx}{\int_0^l \xi^2(x)dx} \frac{1}{Sc} \frac{1}{St^2} \tag{2.75}$$

where Sc is the Scruton number and St is the Strouhal number. The integral of the coefficient c_F over the whole length of the bridge can be approximated by the integral of its maximum value over the correlation length, leading to

$$\int_0^l c_F(x)\xi(x)dx = c_{lat} k_p \int^{L'} \xi(x)dx \tag{2.76}$$

where c_{lat} is the variance of c_F and k_p is the peak factor, the product of both substituting c_F. The peak factor is considered by integrating over an equivalent correlation length L_e longer than the original one, leaving the previous integral as

$$k_p \int^{L'} \xi(x)dx = \int^{L_e} \xi(x)dx \tag{2.77}$$

Therefore, equation 2.75 can reformulated as

$$\frac{y_{max}}{h} = K_w K_\xi c_{lat} \frac{1}{Sc} \frac{1}{St^2} \tag{2.78}$$

where the effective correlation length factor K_w and the mode shape factor K_ξ are

$$K_w = \frac{\int^{L_e} \xi(x)dx}{\int_0^l \xi(x)dx} \qquad K_\xi = \frac{\xi_{max}}{4\pi} \frac{\int_0^l \xi(x)dx}{\int_0^l \xi^2(x)dx} \tag{2.79}$$

It is important to mention that this method has shown to underestimate the vortex shedding response for cases with cold weather and very low turbulence intensity [12]. The model is not able to consider special conditions with very low turbulence, such as the ones encountered in coastal or offshore areas. However, the method is a good approximation for other general cases.

2.5 Aeroelastic effects

In the previous sections the dynamic actions induced by wind's behaviour were explained. Both buffeting and vortex shedding induced loads happen even if the solid is completely static, but the movement of the solid can lead to aditional loads. With sufficiently large deformations of the structure other forces may appear and, for some particular cases, the loads increase with the amplitude of vibration, creating instabilities that can cause the collapse of the structure.

Galloping and *fluttering* are probably the most common aerodynamic instabilities. Despite both of them are self-sustainable, the starting motion needs to be created by lateral buffeting of vortex shedding effects.

2.5.1 Galloping

Galloping is a dynamic instability common in slender and flexible structures with specific cross-sections such a squared or D shapes, where the structure experiences high cross-wind amplitudes of vibrations at frequencies lower than the vortex shedding frequency [38]. When the speed of the solid grows up to a specific point, the aerodynamic damping can become negative (Figure 2.11), increasing even more the oscillations. At some point, the aerodynamic damping gets over the structural damping and the total damping of the system becomes negative [41], leading to the collapse of the structure.

Galloping is very typical in cables due to its flexibility and lightness, but can happen also in other slender structures. The critical wind speed where galloping occurs can be increased by increasing

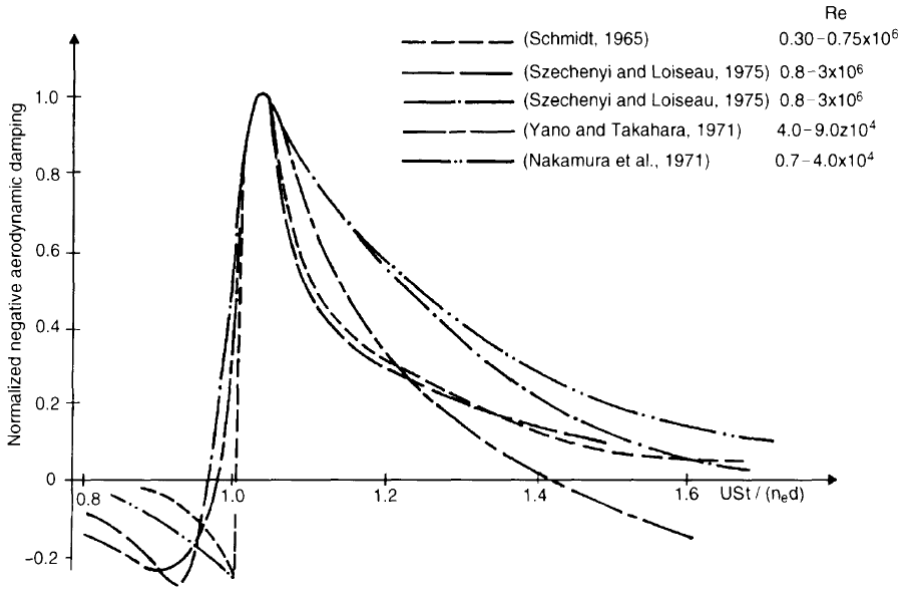

Figure 2.11: Aerodynamic damping depending on the relative frequency of vortex shedding. With frequencies of vortex shedding slightly above the natural frequency of the structure, the aerodynamic damping becomes negative and galloping phenomenon can start. Note that the resulting vibrations will have a lower frequency than the vortex shedding frequency. Source: Vickery, 1978 [46].

the mass or the damping of the structure [12].

Furthermore, the effects of galloping are increased when more than one body is in the same area. The turbulence contained in the wake of a body increases the liberty of oscillation for the bodies behind it, being the phenomenon more likely to happen [38].

2.5.2 Fluttering

Fluttering is usually found in thin and long cross-sections as airfoils or cable supported bridge decks. The phenomenon happens when the first torsional and bending modes of vibrations are coupled [38].

When the bridge deck bends in its first torsional mode of vibration, the angle of attack of the wind changes and the lift coefficient increases considerably. The increased lift coefficient leads to very high amplitudes of vibration, completely synchronized with the torsional vibration [12].

A very visual example of this effect is the collapse of Tacoma Narrows Bridge in 1940. The bridge showed during a long time very large amplitudes of torsional and bending vibration, which finally resulted in the break of its deck.

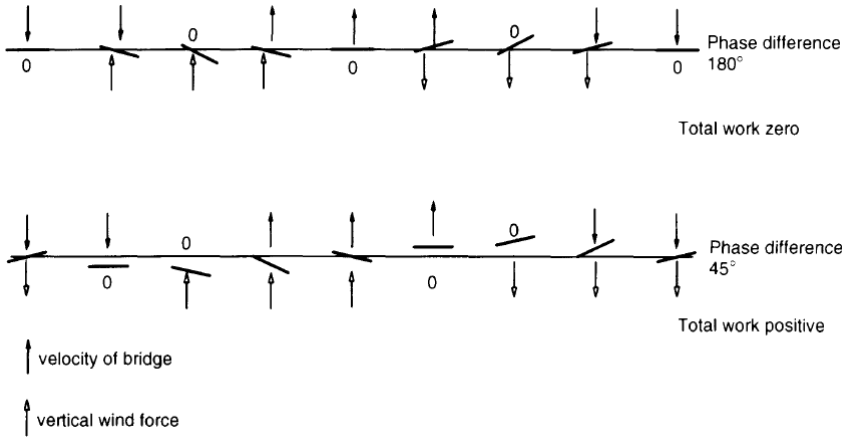

Figure 2.12: Different cases in torsional and bending coupling during fluttering vibrations. Source: *Wind loads on structures* [12].

2.6 Wind loads in Eurocode 1

The European normative regarding wind actions in civil engineering structures is collected in Eurocode 1, part 4 (EN 1991-1-4) [14].

Eurocode 1 is applicable for bridges with spans of less than 200 meters and does not give guidance for torsional vibrations, effects of transversal turbulence, cable supported bridges or other bridges where coupling between mode shapes can occur. Section 8 of the code is dedicated specially to bridges, but only structures with constant section are included.

Regarding the evaluation of dynamic effects induced by the wind, Eurocode states that a dynamic analysis will not be necessary when the span of the bridge is lower than 40 meters. In case that the national annex does not give further information, a dynamic analysis will be necessary for bridges longer than 40 metres. Unfortunately, the methods proposed to analyse the dynamic loads are described in informative annexes, and do not have a legislative nature.

In the following sections, the methods proposed by the code are commented in relation with the concepts explained in the previous questions.

2.6.1 Mean wind speed

The base wind velocity v_b is defined in Eurocode 1 as the characteristic 10 minutes mean wind speed at 10 metres above the ground and in a terrain of category II.

To find the wind-speed at a given height from the ground, the normative uses the logarithmic wind profile (equation 2.4), but with a different notation:

$$\begin{aligned} v_m(z) &= k_r \ln\left(\frac{z}{z_0}\right) v_b \qquad for \quad z \geq z_{min} \\ v_m(z) &= v_m(z_{min}) \qquad\quad for \quad z < z_{min} \end{aligned} \tag{2.80}$$

where z_0 is the roughness length, z is the height above the ground and k_r and z_{min} are parameters

given in a table in the normative depending on the terrain category.

The terms *basic velocity pressure* (q_b) and *peak velocity pressure* (q_p) are also introduced, being the pressure associated with the base wind velocity and the one associated with the wind speed at the given height, including the large eddies effects.

$$q_b = \frac{1}{2}\rho v_b^2 \tag{2.81}$$

$$q_p(z) = [1 + 7I_v(z)]\,\frac{1}{2}\rho v_m^2(z) \tag{2.82}$$

2.6.2 Along-wind response

The force in the along-wind direction of a single element is given in Eurocode as

$$F_w = c_s c_d c_f q_p(z_e) A_r e f \tag{2.83}$$

where z_e is the reference height of the structure, c_f is the force coefficient, equivalent to the drag coefficient for horizontal loading, and $c_s c_d$ is the so-called *structural factor*. The size factor c_s is a favourable coefficient ($c_s \leq 1$) that accounts the lack of correlation between the eddies along the structure, while the dynamic factor c_d takes into account the unfavourable effects of the structure's vibration. The code provides the following formulas to calculate them:

$$c_s = \frac{1 + 7I_v(z_s)\sqrt{B^2}}{1 + 7I_v(z_s)} \qquad c_d = \frac{1 + 2k_p I_v(z_s)\sqrt{B^2 + R^2}}{1 + 7I_v(z_s)\sqrt{B^2}} \tag{2.84}$$

where k_p is the peak factor, $I_v(z_s)$ is the turbulence intensity and B^2 and R^2 are the background and resonance response factors. For non-dynamic cases the factor $c_s c_d$ is taken as 1. Substituting equations 2.82 and 2.84 in equation 2.83 it can be extracted the gust factor assumed in the code:

$$F_w = \left(1 + 2k_p I_v(z_s)\sqrt{B^2 + R^2}\right)\frac{1}{2}\rho v_m^2(z_e) \tag{2.85}$$

$$\varphi = 1 + 2k_p I_v(z_s)\sqrt{B^2 + R^2} \tag{2.86}$$

evidencing that B^2 and R^2 are k_b and k_r, the same parameters explained in section 2.3. The normative gives two possible approaches to calculate k_p, B^2 and R^2 in its informative appendixes B and C.

Procedure 1

The integral length scale assumed in Eurocode 1 has the following expression:

$$\begin{aligned} L(z) &= L_t \left(\frac{z}{z_t}\right)^{\alpha} \qquad for \quad z \geq z_{min} \\ L(z) &= L(z_{min}) \qquad for \quad z < z_{min} \end{aligned} \tag{2.87}$$

$$\alpha = 0.67 + 0.05\ln(z_0) \tag{2.88}$$

where $z_t = 200\,m$ is a reference height, $L_t = 300\,m$ is the length scale at the reference height z_t and z_{min} is the same parameter used for the calculation of the logarithmic profile. Knowing the integral length scale, the background factor is calculated as

$$B^2 = \frac{1}{1 + 0.9\left(\frac{b+h}{L(z_s)}\right)^0 .63} \tag{2.89}$$

where b and h are the width and height of the structure. Regarding the resonance response factor, the formula given by Eurocode 1 is very similar to the one explained before (equation 2.62):

$$R^2 = \frac{\pi^2}{2\delta} S_L(z_s, n_{1,x}) R_b(\eta_b) R_h(\eta_h) \tag{2.90}$$

where $R_b(\eta_b)$ and $R_h(\eta_h)$ are the aerodynamic admittance functions for the horizontal and vertical direction respectively and $S_L(z_s, n_{1,x})$ is the non-dimensional power spectral density function. For the last one, the normative uses the formula proposed by Kaimal *et al.* [20] described in equation 2.20. For an horizontal line-like structure as a bridge $R_h(\eta_h) = 1$, and the horizontal admittance function can be approximates as

$$R_b(\eta_b) = \frac{1}{\eta_b} - \frac{1}{2\eta_b^2}\left(1 - e^{-2\eta_b}\right) \tag{2.91}$$

$$\eta = \frac{4.6b}{L(z_s)} f_L(z_s, n_{1,x}) \tag{2.92}$$

where $n_{1,x}$ is the natural frequency of the structure and $f_L(z_s, n_{1,x})$ is the non-dimensional frequency given in equation 2.15. By last, the peak factor k_p is calculated in Eurocode 1 with a slight variation in Euler's constant γ and the up-crossing frequency ν, resulting in the following expressions:

$$k_p = \sqrt{2\ln(\nu T)} + \frac{0.6}{\sqrt{2\ln(\nu T)}} \tag{2.93}$$

$$\nu = n_{1,x}\sqrt{\frac{R^2}{B^2 + R^2}} \tag{2.94}$$

where $T = 600\,s$ is the averaging time for the mean wind speed.

Procedure 2

The second procedure uses the same equations to calculate the integral length scale $L(z_s)$ and the peak factor k_p than in the first procedure. Nevertheless, varies in the calculation of the background factor B^2 and the resonance factor R^2. Eurocode 1 uses in this case the expressions first published by Dyrbye *et al.* [12], already explained in section 2.3.

2.6.3 Cross-wind response

Eurocode 1 proposes in an informative annex two alternative methods to calculate the vortex shedding response. On the one hand, uses the method proposed by Ruschewyh explained in section

2.4.3, and on the other hand, proposes an alternative method only applicable for cantilevered structures with constant distribution of cross-wind dimension. The last one allows the consideration of different turbulence intensities, being specially adequate for cases with extremely low turbulence, such as coastal structures, where the first method may underestimate the response. However, in order to analyse the type of bridge assessed in this report, only the first model is applicable.

The code uses the same formulation explained in section 2.4.3, but with a slightly different notation. Furthermore, it proposes some values for the parameters K_w and K_ξ for simple structures. In the case of single span bridges, $K_\xi = 0.10$ for simply supported beams and $K_\xi = 0.11$ for beams with clamped edges. Regarding, the effective correlation length factor K_w, Eurocode 1 proposes an iterative method to calculate it. The equations applicable for bridges are:

$$\text{Simply supported beams} \quad \rightarrow \quad K_w = \cos\left[\frac{\pi}{2}\left(1 - \frac{L_j/b}{l/b}\right)\right] \tag{2.95}$$

$$\text{Beams with clamped edges} \quad \rightarrow \quad K_w = \frac{L_j/b}{l/b} + \frac{1}{\pi}\sin\left[\pi\left(1 - \frac{L_j/b}{l/b}\right)\right] \tag{2.96}$$

where l is the length of the structure, b its width, and L_j the equivalent correlation length. The ratio L_j/b is given by the following formulas:

$$\begin{aligned} \frac{L_j}{b} &= 6 \quad \text{for} \quad 0.1 < fracy_F(s_j)b \\ \frac{L_j}{b} &= 4.8 + 12\frac{y_F(s_j)}{b} \quad \text{for} \quad 0.1 > \frac{y_F(s_j)}{b} > 0.6 \\ \frac{L_j}{b} &= 12 \quad \text{for} \quad \frac{y_F(s_j)}{b} > 0.6 \end{aligned} \tag{2.97}$$

where the ratio $y_F(s_j)/b$ is the same as y_{max}/h in equation 2.78. The previous equations are solved with the along with equation 2.78 in an iterative way until reaching the solution.

Eurocode 1 also provides a table with values of the Strouhal number St and lateral coefficient c_{lat} for different shapes. Unfortunately, the values for the I beam with wind in the lateral direction is not provided, being necessary to calculate it with computational help of wind tunnel tests. Moreover, the code makes a correction of the lateral coefficient, assuming that extreme winds will not last enough time to excite completely the structure [12]. The correction is given by the following expressions:

$$\begin{aligned} c_{lat} &= c_{lat,0} \quad \text{for} \quad 0.83 \leq \frac{v_{crit}}{v_{m,L_j}} \\ c_{lat} &= \left(3 - 2.4\frac{v_{crit}}{v_{m,L_j}}\right) c_{lat,0} \quad \text{for} \quad 0.83 \leq \frac{v_{crit}}{v_{m,L_j}} \leq 1.25 \\ c_{lat} &= 0 \quad \text{for} \quad \frac{v_{crit}}{v_{m,L_j}} \leq 1.25 \end{aligned} \tag{2.98}$$

where $c_{lat,0}$ is the initial lateral coefficient given in the tables, v_{crit} is the wind speed that causes the resonance of the structure and $v_{m,Lj}$ is the mean wind speed in the middle of the correlation length. By last, Eurocode 1 translates the maximum deflection y_{max} into forces by the following formula, assuming that the mode force is proportional to the mode shape function if the mass is constant:

$$F_w(s) = m(s) \left(2\pi n_{i,y}\right)^2 \Phi_{i,y(s)} y_{max} \tag{2.99}$$

where s is the location along the structure, $F_w(s)$ is the wind induced force per unit length, $m(s)$ is the mass per unit length, $n_{i,y}$ is the natural frequency of the structure, $\Phi_{i,y(s)}$ is the normalised mode shape and y_{max} is the maximum deflection of the structure.

Chapter 3

Method

3.1 Model description

In order to obtain the dynamic wind effects on the structure, several geometries were tested with the CFD software Ansys-Fluent.

The complexity of the vortex shedding phenomenon makes it very difficult to perform a parametric study with 3D simulations so the analysis was carried out with 2D simulations, focussing on the shape of the cross-section. Even though the vortex shedding can change in the zones near the supports of the bridge, the important actions for the structural response are the ones in the middle zones of the span. Therefore, the calculation of the important parameters of the wind flow for a representative section was considered to be enough for the scope of this master thesis.

The parameters studied in the simulations were four (Figure 1.1): the height of the cross section of the beams (h), the distance between them (d), the width of their flanges (b) and the distance between the floor and the lowest point of the beams (H).

In order to consider the free flow conditions in the upwind, downwind and upper directions, the model needs to be extended a considerable distance. Modelling the free flow boundaries too near from the analysed geometry would lead to blockage effects and inaccuracies in the definition of the input and output flows [44]. The distance finally taken for the upwind and upper directions was 120 meters, while the model extended for 150 metres in the downwind direction.

3.1.1 Parametric study

Three different situations were considered in the parametric analysis (Figure 3.1). First, the case when only one beam is placed, second, the stage when both beams are in their locations, and by last, the case were both beams are placed but the space between them is isolated from the external flow with wood or steel plates. The last case was included to see if any improvement is observed in the aerodynamic parameters of the section, being then a possible solution to reduce the vulnerability of the section.

Regarding the parameters previously mentioned, three different values were assigned to the height

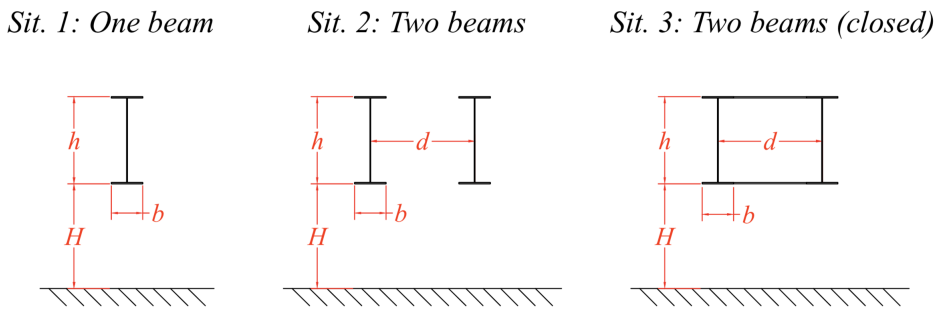

Figure 3.1: Construction stages considered in the parametric study.

of the section (h), the distance between beams (d) and the height of the bridge (H). The width of the flanges is usually conditioned by the joint procedure with the concrete slab, so it was assumed a constant value of $b = 0.9\,m$.

The height of the beams for simple girder bridges with spans around 40 metres varies between 2 and 3 metres, so the values of $h = 2\,m$, $2.5\,m$, $3\,m$ were tested. Regarding the distance between beams, usually it is equal or bigger than the height of the section, so the values were taken depending on the last one, leaving $d = h + 0\,m$, $h + 0.5\,m$, $h + 1\,m$. By last, the height of the bridge was assumed to be $H = 3\,m$, $5\,m$, $10\,m$, usual heights for this type of bridges. Furthermore, an additional height of $H = 120\,m$ was considered, representing the free flow. Therefore, for the first situation 12 different geometries were tested, while for the second and third situations, 36 cases were analysed.

Moreover, each case was simulated with different wind speeds in order to obtain the mean results, reducing the uncertainty of the final value. Besides, simulating different speeds was useful to check that the results were Reynolds-independent. For the first situation the wind speeds $U = 2.5\,m/s$, $5\,m/s$, $7.5\,m/s$, $10\,m/s$, $12.5\,m/s$, $15\,m/s$, $20\,m/s$, $30\,m/s$ were considered, while for the situations with both beams only the wind speeds in the range of $5 - 10\,m/s$ were tested.

In conclusion, a total of 456 simulations were needed to test all the combinations of parameters.

3.1.2 Physics configuration

The density of the air was assumed to be $\rho_a = 1.225\ kg/m^3$, while the dynamic viscosity was assumed to be $\mu = 1.7894 \cdot 10^{-5}$, corresponding with a temperature around 15^oC [43]. As the air is not a dense fluid and the variation of height in the structure is very low, the simulations were made neglecting the effects of gravity in the fluid's behaviour.

About the boundary conditions, the contour of the beams and the lower part of the model –symbolizing the floor– were defined as walls, with zero speed in the tangential and normal direction. The upper part of the model –symbolizing the free air– was defined as a symmetry boundary condition to avoid the formation of a boundary layer, while the outlet was set with a zero pressure condition. Finally, in the upwind extreme of the model, the inlet was defined as a constant wind speed in all the segment, with the values discussed in section 3.1.1.

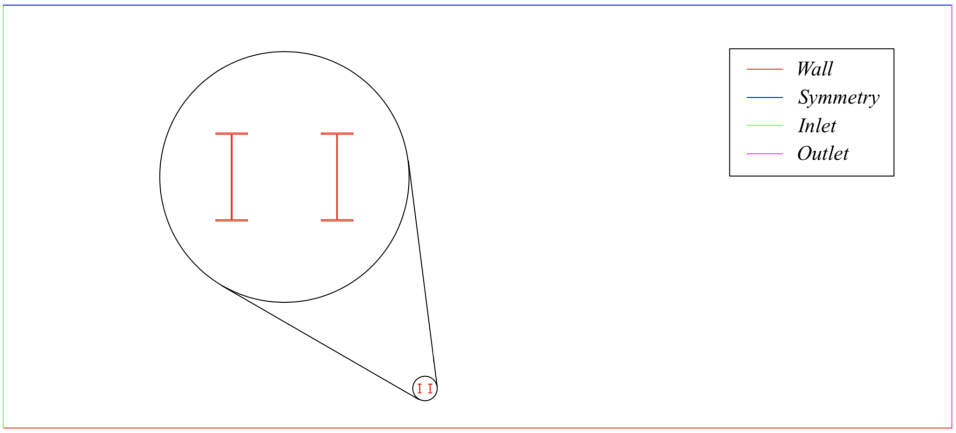

Figure 3.2: Definition of the boundary conditions in the model.

3.1.3 Mesh

The meshing procedure was made with the software Ansys-ICEM, and it is composed of quadrilateral elements. A quadrilateral mesh is more difficult to build and less flexible, but when the flow is aligned with one of the directions of the cells, the model requires less computational time than with a triangular mesh. Besides, the use of quadrilateral cells in the near-wall zones is highly recommended [44].

An hybrid mesh with quadrilateral cells in the near-wall zones and triangular cells in the rest of the model was also possible. Nevertheless, the automatic mesh generator formed very skewed cells in the corners of the beams, just were the flow needed to be defined with accuracy. Therefore, the mesh was finally generated manually with blocking procedures.

The cell size perpendicular to the wall in the surfaces was set in 1 mm. As the model is using wall functions to simulate the flow near the surfaces, this size is small enough to obtain acceptable results. The change ratio between adjacent cells was set in 1.2, ensuring smooth transitions between the cells in the surface and the rest of the fluid domain. In Figure 3.3 the size of the cells near the walls and the treatment of the section's corners can be observed.

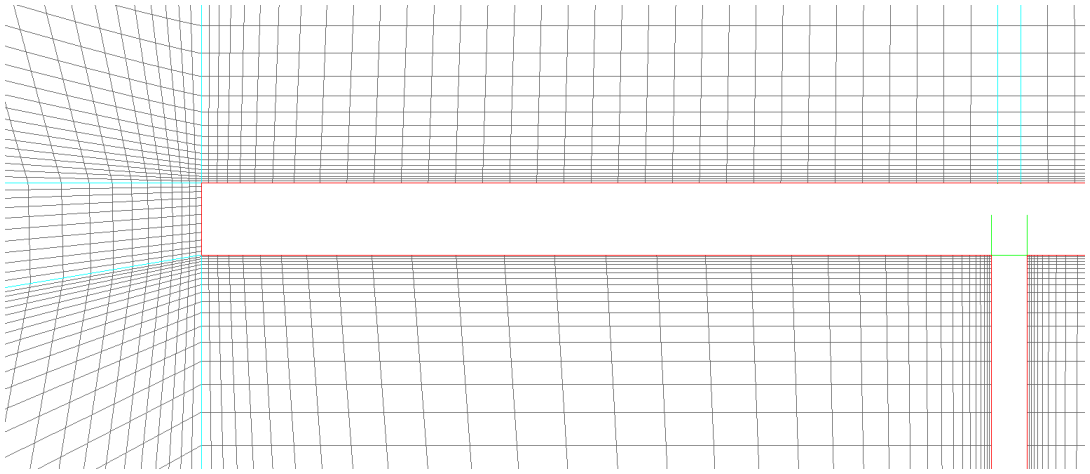

Figure 3.3: Mesh around the corners and in the walls.

Cell size is then increased constantly using radial structures to fill all the surface of the model with the minimum number of elements possible, avoiding always strong changes in cell's size and elements with angles below 45^o or above 135^o. Moreover, the formation of the vortexes in the wake of the body has a great impact in the drag, lift and Strouhal coefficients. In order to allow the correct development of the wake, it was necessary to maintain cell's size in low values in the downwind zone of the beams' cross-section (Figure 3.4).

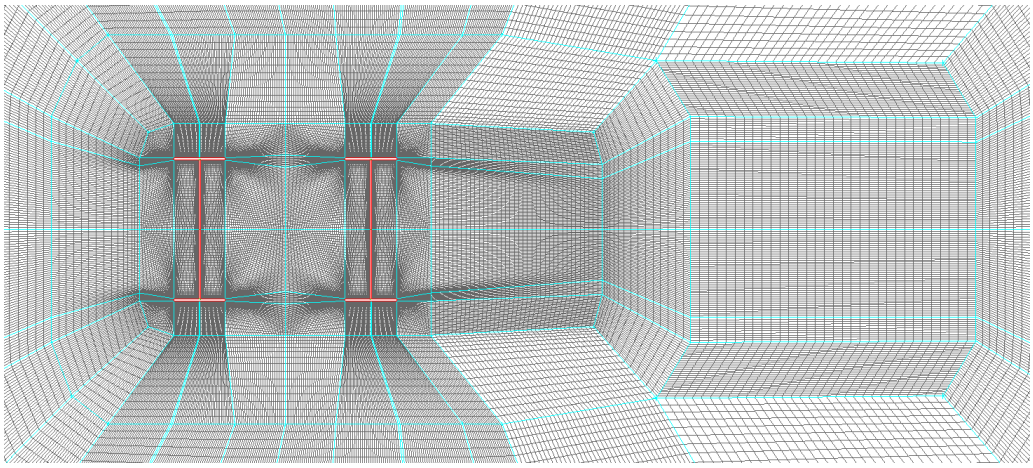

Figure 3.4: Mesh structure for the case with $h = 2.5\,m$, $d = 3\,m$ and $H = 120\,m$. Note that the disposition of the blocks (light blue) maintain moderate element sizes in the beginning of the wake zone.

The manual generation of the described mesh is quite time-consuming, so it was necessary to script the process in Tcl, the string-based programming language used by ICEM (see Appendix B). As the number of cells attached to a segment depends on its length, the total number of elements in the model changes considerably with the geometry tested. The smaller models –found in cases with only one beam– had around 110.000 elements, whereas the bigger ones –in cases with both beams in their location– had approximately 195.000 elements. However, all models have the same element size in the zones surrounding the shapes.

3.1.4 Solver parameters

As the von Kármán vortex street is a time-dependent phenomenon, a transient formulation was used in the simulations. The second-order transient simulation solver was used to improve accuracy. The maximum number of iterations per time step was set in 200 to ensure a full convergence in every time step.

The time step and the total time of simulation for each case depends on the wind speed tested. First, for high speeds the frequency of vortex shedding increases, being possible to capture the same number of cycles in less simulation time. Second, it is necessary to have at least 100 time steps per cycle, so the faster the phenomenon is, the smaller the time step should be.

Furthermore, it is necessary to consider a certain time at the beginning of the simulation to let the flow find a stable cyclic behaviour. After this time, the time series can be analysed in the frequency domain to find the Strouhal number. In order to reduce this stabilization time and increase the analysable time, 10000 iterations with the steady state solver were made before each transient

simulation. Due to the instability of the flow with these Reynolds numbers, the steady state solver cannot converge, but is useful to give the transient solver a start near to the final behaviour.

Finally, the settings showed in Table 3.1 were chosen, being enough to reproduce sufficient cycles of drag and lift forces to make an accurate estimation of all the parameters.

Wind speed (m/2)	2.5	5	7.5	10	12.5	15	20	30
Time step (s)	0.04	0.02	0.012	0.01	0.008	0.006	0.005	0.0032
Time of simulation (s)	240	120	72	60	48	36	30	19.2
Number of time steps	6000	6000	6000	6000	6000	6000	6000	6000

Table 3.1: Transient solver parameters chosen depending on the wind speed tested.

Regarding the turbulence treatment, the $k-\epsilon$ model was used in all the simulations. As it is a Reynolds-Average Navier-Stokes (RANS) model, the accuracy is lower than using Direct Numerical Simulation (DNS) or Large-Eddie Simulation (LES) models, but the computational time is much lower, and the results are enough to make a qualitative assessment of the flow [44]. Furthermore, LES and DNS models have more strict mesh conditions, increasing even more the computational time and the difficulties to calibrate and validate the model.

Particularly, the Re-Normalization Group (RNG) variation of the $k-\epsilon$ model proposed by Yakhot *et al.* [52] was used, with an enhanced wall treatment to simulate the flow near the surfaces. The parameters of the model were the default ones proposed by the software: $C_\mu = 0.0845$, $C_{\epsilon 1} = 1.42$ and $C_{\epsilon 2} = 1.68$.

3.1.5 Extraction of the results

Seven different non-dimensional coefficients were extracted from the simulations to make the assessment of the section's behaviour:

- The Strouhal number (St).
- The mean values of the drag, lift and moment coefficients (C_D,C_L,C_M).
- The Root Mean Square (RMS) values of the drag, lift and moment coefficients ($\overline{C}_D$,$\overline{C}_L$,$\overline{C}_M$), representing their variances.

The drag and lift forces can be obtained integrating the pressure along the surface of the shape immersed in the flow:

$$\overrightarrow{F} = \oint -p_s \overrightarrow{n} dS \tag{3.1}$$

where $\overrightarrow{F}$ is the resultant force, p_s is the static pressure of the fluid, $\overrightarrow{n}$ is the unitary vector perpendicular to the surface S. As CFD entails the discretization of time and space in the model, the static pressure can only be obtained for each cell in the boundary of the cross-section. Drag and lift forces in a 2D model can be extracted then as

$$F_D = \sum_{i=1}^{k} -p_{s,i} n_{x,i} s_i \tag{3.2}$$

$$F_L = \sum_{i=1}^{k} -p_{s,i} n_{y,i} s_i \tag{3.3}$$

where F_D and F_L are the drag and lift forces, k is the number of cells in the contour of the shape, s_i is the surface of the cell in contact with it and $n_{x,i}$ and $n_{y,i}$ are the components of n. By last, the resulting moment can also be calculated with a similar procedure:

$$M = \sum_{i=1}^{k} p_{s,i} s_i \left(n_{x,i}(y_i - y_G) - n_{y,i}(x_i - x_G) \right) \tag{3.4}$$

where x_G and y_G are the coordinates of the centroid of the cross-section and x_i and y_i are the coordinates of the cell i. Therefore, the values of the static pressure in all the cells in the contour of the beams was exported from Fluent in ASCII format for each time step, and it was processed later by a Matlab code to obtain the drag, lift and moment coefficients time-series.

It is important to mention that the viscosity of the fluid also causes a tangential force to appear around the body. However, with low-viscosity fluids as the air, the tangential forces are much lower than the normal forces generated by the pressure. These forces are important to consider in streamlined bodies such as airfoils, but can be neglected in cases as the analysed in this report.

About the Strouhal number, the coefficient can be easily extracted from the frequency domain of the lift force. The change from time domain to frequency domain was made with the Fast Fourier Transform (FFT) method, already implemented as a Matlab function. In order to improve the accuracy of the results using the FFT, the zero-padding method was used. Therefore, the precision of the results was improved without increasing the time of simulation.

3.2 Verification of the model

The verification of the model is usually done in these cases with wind-tunnel tests, which is not available for the development of the present thesis. It is necessary then to compare the results obtained from the computational simulations with results found in the literature. As said in section 1.1, the main part of the research in the field has been focussed in simple geometries as circular or squared cylinders, making difficult to find results for the aerodynamic properties of I beams. It is necessary then to check the model with a simple geometry before starting with the parametric study.

The geometry chosen to make the validation was a flat plate perpendicular to the flow. Even though the case is not as studied as circular shapes, several articles can be found in the literature about it. Furthermore, the bluffness of this shape is quite similar to an I beams, with sharp corners and a high height-width ratio.

3.2.1 Geometry description

In order to find the base aerodynamic parameters of the flat plate, the shape was situated in the middle of the model, with symmetrical boundary conditions in the upper and lower edges of the model.

The flat plate finally tested was 2.5 metres height and 2 cm width, and the mesh of the model was made with the same conditions explained in section 3.1.3 to ensure that the validation of this geometry is useful for the other models. In Figure 3.5 can be observed a detail of the mesh in the zone near to the body, again with a denser mesh in the downwind direction.

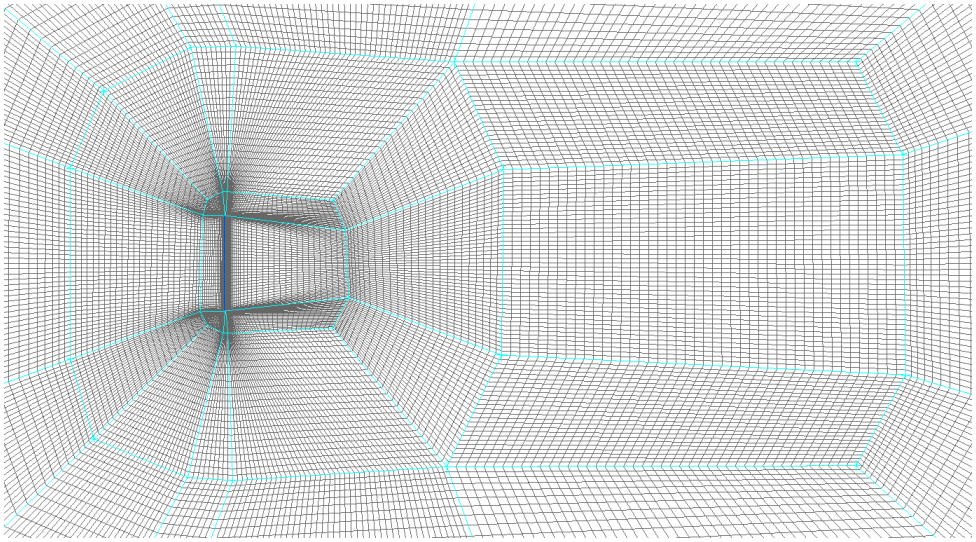

Figure 3.5: Mesh around the solid defined for the validation geometry.

3.2.2 Grid and time step convergence tests

In every CFD model it is necessary to make a grid and a time step convergence test to ensure that the space and time discretization is a good approximation of the reality. In order to do that, the number of elements of the model and its time step is changed until the results remain constant. For each variation, the Strouhal number, the mean drag coefficient and RMS value of the drag coefficient were calculated to check the influence of mesh and time step.

Grid convergence test

The starting model of the flat plate had 42000 elements and it was increased by steps of approximately a 30% of the initial number. The increase of the total number of elements was made with the help of the software ICEM, which allows the user to increase the mesh density in all the model respecting different densities in the starting model.

Finally, 6 different models were tested, with a total number of elements of 42000, 55000, 68000, 81000, 94000 and 107000. The different versions were tested with two wind speeds: $U = 5\,m/s$ and $U = 15\,m/s$. Regarding the time step, $\Delta t = 0.02\,s$ was set for the low wind speed simulations ($U = 5\,m/s$) and $\Delta t = 0.006\,s$ for the ones with high wind speed ($U = 15\,m/s$), ensuring to have

around 200 time steps per cycle of vortex shedding. The results obtained with these settings are shown in Table 3.2.

Nº elements			42000	55000	68000	81000	94000	107000
Wind speed = 5 m/s	Strouhal number	Value	0.123	0.123	0.123	0.123	0.123	0.124
		Err. Prev. (%)		0.00	0.00	0.00	0.00	0.81
		Err. Final (%)	0.81	0.81	0.81	0.81	0.81	
	Drag coefficient	Value	2.7131	2.7144	2.7172	2.7124	2.709	2.7102
		Err. Prev. (%)		0.05	0.10	0.18	0.13	0.04
		Err. Final (%)	0.11	0.15	0.26	0.08	0.04	
	RMS Drag coefficient	Value	0.2202	0.2195	0.2212	0.2186	0.2166	0.2146
		Err. Prev. (%)		0.32	0.77	1.18	0.91	0.92
		Err. Final (%)	2.61	2.28	3.08	1.86	0.93	
Wind speed = 15 m/s	Strouhal number	Value	0.121	0.121	0.121	0.122	0.122	0.122
		Err. Prev. (%)		0.00	0.00	0.83	0.00	0.00
		Err. Final (%)	0.82	0.82	0.82	0.00	0.00	
	Drag coefficient	Value	2.7094	2.7139	2.7189	2.7189	2.72	2.7237
		Err. Prev. (%)		0.17	0.18	0.00	0.04	0.14
		Err. Final (%)	0.53	0.36	0.18	0.18	0.14	
	RMS Drag coefficient	Value	0.224	0.223	0.2248	0.2213	0.2197	0.2182
		Err. Prev. (%)		0.45	0.81	1.56	0.72	0.68
		Err. Final (%)	2.66	2.20	3.02	1.42	0.69	

Table 3.2: Results of the grid convergence test. *Err.Prev.* refers to the change between a mesh and the previous one, whereas *Err.Final.* refers to the error respect to the model with more number of elements.

All the errors are under 5%, so the model can be assumed to be mesh-independent. For further analysis, the mesh with 55000 elements was used. It is important to note that, even though the number of elements differ considerably from the ones explained in section 3.1.3, the geometric characteristics of the elements have been maintained. Thus, element sizes are the same, but the complexity of the geometries in the parametric study increases the total number of elements.

Time step convergence test

When analysing the von Kármán vortex street phenomenon, it is recommended to simulate at least 100 time steps per vortex shedding cycle to have accuracy in the calculation of the Strouhal number. Thus, as the vortex shedding frequency changes with wind velocity, the time step size will vary also with it.

For the time step convergence test five simulations were made with both wind speeds, corresponding with 50, 100, 200, 400 and 800 approximate time steps per cycle. Therefore, the simulations with $U = 5\,m/s$ were made with $\Delta t = 0.08\,s,\ 0.04\,s,\ 0.02\,s,\ 0.01\,s,\ 0.005\,s$, while the simulations with $U = 15\,m/s$ were made with $\Delta t = 0.024\,s,\ 0.012\,s,\ 0.006\,s,\ 0.003\,s,\ 0.0015\,s$.

It is important to note that, as the final Strouhal number is not known, the number of time steps per cycle is an approximation. A high Strouhal number would entail less time steps per cycle. The parameters obtained with the mentioned settings are shown in Table 3.3.

The final number of time steps per cycle chosen was 200. Even though 100 time steps per cycle showed also acceptable results, with the beam models the Strouhal coefficient might increase, reducing this number.

Aproximate time steps per cycle			50	100	200	400	800
Wind speed = 5 m/s	Time step size (s)		0.08	0.04	0.02	0.01	0.005
	Strouhal number	Value	0.122	0.122	0.123	0.123	0.123
		Err. Prev. (%)		0.00	0.82	0.00	0.00
		Err. Final (%)	0.81	0.81	0.00	0.00	
	Drag coefficient	Value	2.7533	2.7356	2.7204	2.7138	2.7122
		Err. Prev. (%)		0.64	0.56	0.24	0.06
		Err. Final (%)	1.52	0.86	0.30	0.06	
	RMS Drag coefficient	Value	0.20748	0.213	0.2176	0.2198	0.2207
		Err. Prev. (%)		2.66	2.16	1.01	0.41
		Err. Final (%)	5.99	3.49	1.40	0.41	
Wind speed = 15 m/s	Time step size (s)		0.024	0.012	0.006	0.003	0.0015
	Strouhal number	Value	0.121	0.121	0.121	0.121	0.121
		Err. Prev. (%)		0.00	0.00	0.00	0.00
		Err. Final (%)	0.00	0.00	0.00	0.00	
	Drag coefficient	Value	2.7312	2.7356	2.7204	2.7138	2.7122
		Err. Prev. (%)		0.16	0.56	0.24	0.06
		Err. Final (%)	0.70	0.86	0.30	0.06	
	RMS Drag coefficient	Value	0.21337	0.2185	0.2223	0.2242	0.225
		Err. Prev. (%)		2.40	1.74	0.85	0.36
		Err. Final (%)	5.17	2.89	1.20	0.36	

Table 3.3: Results of the time step convergence test. *Err.Prev.* refers to the change between a mesh and the previous one, whereas *Err.Final.* refers to the error respect to the model with more number of elements.

3.2.3 Verification

The verification of the model was made comparing the results of the drag coefficient and the Strouhal number with literature data.

In 1954, Roshko made measurements of aerodynamic characteristics of bluff-bodies with Reynolds numbers in the range of $3 \cdot 10^3 < Re < 2 \cdot 10^4$, obtaining Strouhal numbers for the flat plate between $St = 0.133$ and $St = 0.14$ [30]. Later, Chen *et al.* made wind-tunnel tests of flat plates with Reynolds numbers between $Re = 3.5 \cdot 10^3$ and $Re = 3.2 \cdot 10^4$, obtaining a Strouhal number of $St = 0.16$ [2]. After doing the correction of the blockage effect the result obtained was $St = 0.136$. However, Simiu *et al.* gave a Reynolds-independent value of $St = 0.145$ [38].

The Strouhal number obtained with the model after the grid and time step convergence test is $St = 0.121$, with an error of approximately 10-20%. The approximation is useful for many engineering purposes, such as the parametric study carried out in the present master thesis. Errors of this size are expectable from CFD simulations [10], specially if this project is limited to the use of RANS turbulence models.

Regarding the drag coefficient, Simiu *et al.* expose $C_D = 1.96 - 2.01$ [38], while Hoerner states $C_D = 1.98$ [19]. The extracted value for the simulations is $C_D = 2.72$, with a 35% of error. However, the results are still in the expected range from simulations with the $k - \epsilon$ turbulence model.

In Table 3.4, a summary of the mentioned results for the Strouhal number and Drag coefficient is shown.

	Roshko	Chen *et al.*	Simiu *et al.*	Hoerner	Model
Strouhal number	0.133-0.140	0.136	0.145	-	0.121
Drag coefficient	-	-	1.96-2.01	1.98	2.72

Table 3.4: Values of the Strouhal number and drag coefficient given by Roshko [30], Chen *et al.* [2], Simiu *et al.* [38] and Hoerner [19] in comparison with the results obtained from the model.

3.3 High computing performance

With the simulations settings previously mentioned, each simulation takes around 6-8 hours in a regular computer. To do all 456 of them would be necessary to be running the models in a computer for 4-5 months. It is necessary then to use high performance computing methods to carry out this project in a viable time.

Fortunately, the Royal Institute of Technology has the Center for High Performance Computing (PDC), with two supercomputers, being one of them the faster in all Nordic countries. The main function of PDC is to provide computational services for academic research, but it also can be used by the private sector.

PDC manages two different supercomputers: Beskow and Tegner. Beskow is the main cluster of the centre and one of the fastest computers in Europe, with a total of 67456 cores distributed among 2060 nodes. About Tegner, it is usually used for pre- and post- processing tasks for Beskow, but it can also be used to run small and medium jobs. It has 1800 cores distributed among 65 nodes, with the main part of the nodes having 24 cores.

All the simulations needed for this study were made using Tegner computer. This sections explains some operation aspects regarding high computing performance and the organization scheme followed to systematize the calculations.

3.3.1 Parallelization of the simulations

The advantage of running in clusters relies in the parallelization of the jobs, and not only in the increased speed of each core. Different processes can be run in different cores, reducing the total computing time. Usually, simulation programs such as Ansys allow to parallelize the tasks, but depending in the type of simulation, the saved time can vary.

For two-dimensional fluid simulations the parallelization of the tasks is not as efficient as in 3D cases. In other words, using several cores in parallel will save time, but the total computational time is not inversely proportional to the number of cores used. Thus, when running the needed simulations in a Tegner's node with 24 cores, the computational time will only be reduced by two or three.

Nevertheless, in this case the problem is not the computational time of one simulation, but the total number of simulations needed. It is possible then to run several independent simulations in the same node, allowing each core to be more efficient. Then, the total time of a simulation will not vary, but at the same time several simulations can be made.

The problem of this methodology is the usage of Ansys licenses. Each parallel simulation would be

using a different license, and the total number of them is limited. It was finally necessary to find a point in between. During the parametric study 4 to 8 simulations were run at the same time in a single node, meaning 6 to 3 cores per simulation respectively.

3.3.2 Organization of the process

In order to systematize all the process, several scripts were made in Tcl, Python and Matlab. With them, it was possible to reduce the time spent in the parametric study simulations and avoid mismatches between the data.

First of all, the geometry and mesh creations were done in Ansys-ICEM for all the 84 different cases. The scripting was done in Tcl, as is the language used by the program. Afterwards, this geometry was imported in a Fluent file, which had a few basic settings prepared. This file was moved to Tegner computer to proceed with the simulation.

In Tegner it was necessary to build the journal files for each case, where it was indicated the wind speeds to test and the parameters of Fluent's solver. Besides, the generation of a batch file was needed to launch the job and indicate which cases will be run and with how many cores per simulation.

As explained in section 3.1.5, Fluent exported the pressures around the beams for each time step in ASCII files. These files were also processed inside Tegner with a Matlab script, in order to calculate the drag, lift and moment time-series.

By last, the results were saved in Matlab files and extracted again to the personal computer. There, with more Matlab codes, the seven parameters were calculated, and the needed plots could be easily designed. In Figure 3.6 an overview of the whole process is shown, indicating the tasks of each script.

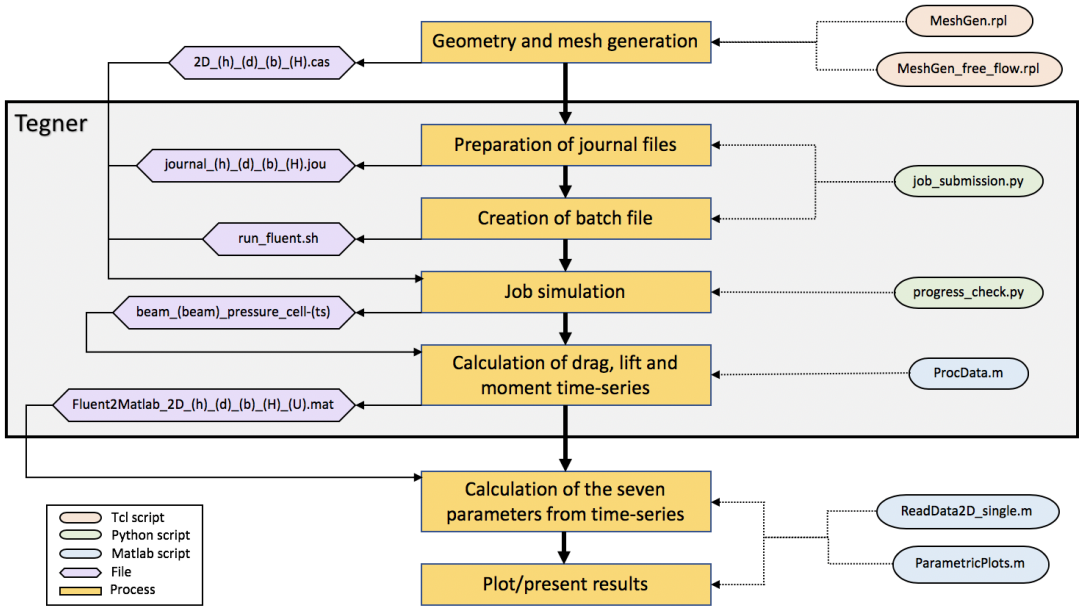

Figure 3.6: Complete process from the definition of the geometry until the extraction of the results. The different scripts can be found in Appendix B.

Chapter 4

Results and discussion

4.1 Situation 1: Single beam

The first thing observed after the extraction of the results was their dependency on the wind speed. As the analysed body has sharp corners, the separation of the boundary layer should be located always in the same point, resulting in nearly constant aerodynamic parameters.

The different parameters showed similar values for all flow velocities except in the simulations with $U = 20\,m/s$ and $U = 30\,m/s$. These last two wind speeds showed slight differences in their results, specially in the case of $U = 30\,m/s$. In Figure 4.1 can be observed how the Strouhal number with high speeds is lower than in other cases.

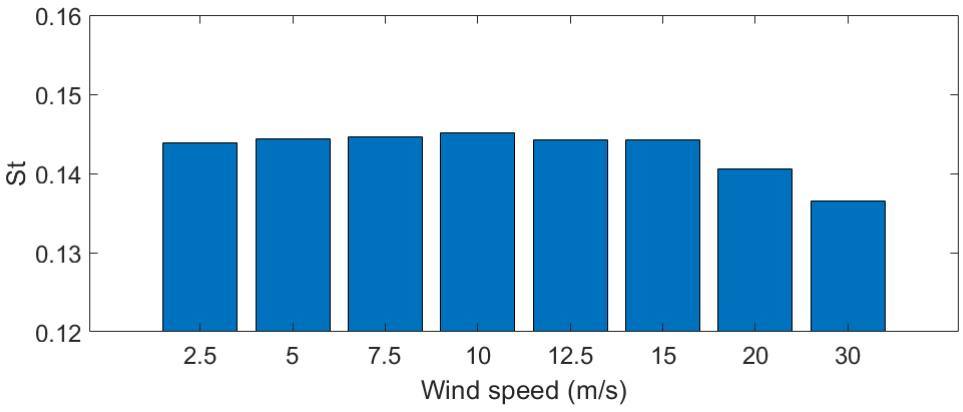

Figure 4.1: Mean values of the Strouhal number obtained with each wind speed in all the single beam simulations.

The differences might be due to the effects of the turbulence. However, the range of wind speeds where vortex shedding effects are more probable to happen is $U = 5 - 15\,m/s$ [16], so the analysis was focussed on the Reynolds-independent values given by the simulations with velocities in this range.

In the following sections, the Strouhal number, drag coefficient and RMS values of the drag and lift coefficient are commented. The lift and moment coefficient were considered of less importance

because, due to the symetry of the cross-section, they are approximately zero. Regarding the RMS value of the torsional coefficient, the results showed also that its values are low for the single beam situation. All the analysed results are based then in the simulations with wind speeds between $5\,m/s$ and $15\,m/s$.

Strouhal number and drag coefficient

The Strouhal number and drag coefficients are parameters strongly related. Variations in one of them can be seen also in the other [30]. Their values obtained for the 12 different geometries of the single beam case are shown in Figure 4.2.

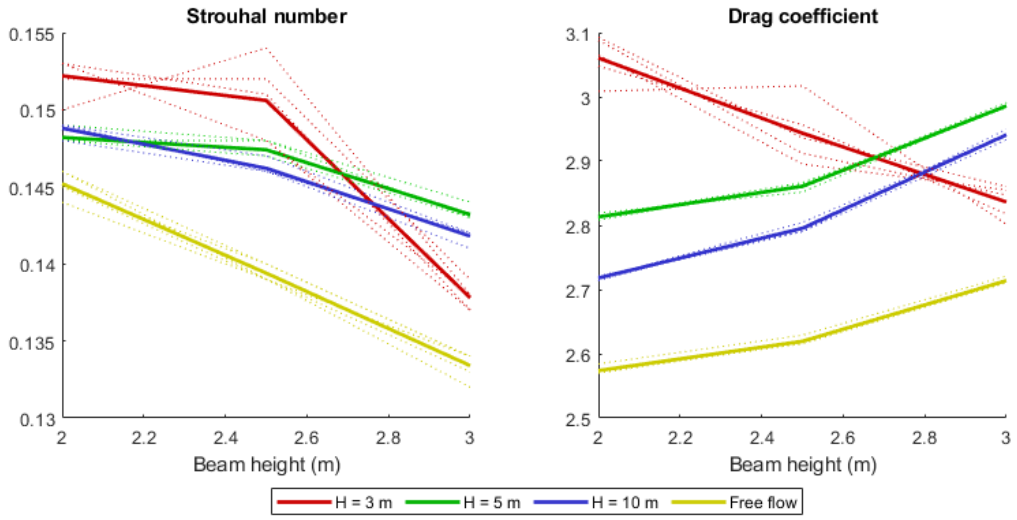

Figure 4.2: Values of the Strouhal number and drag coefficient extracted from the simulations with one beam. The dotted lines represent the results for a particular wind speed, while the continuous lines are the average values from all the wind speeds.

It can be observed that the simulations with a bridge's height $H = 3m$ do not follow the same path as the rest of the simulations. Moreover, the simulations gave very different results with different wind speeds, showing irregularities. These results were attributed to the influence of the ground on the von Kármán vortex street. If the surface is too close, the wake might be affected, disturbing the development of the phenomenon. Figure 4.3 shows the vorticity in a simulation with $H = 3\,m$ for a particular moment. In it, it can be seen how the wake is displaced upwards, breaking its symmetry.

Another conclusion that can be indirectly extracted from the results is that beam's width has an influence in both coefficients. This can be observed in the results of the simulations in free flow. A higher section means a thinner beam in proportion, and as the coefficients depend on the shape and not in the size of the body, the changes should be caused by beam's width.

Regarding the influence of h, a higher beam height –or a thinner beam width in proportion– implies a lower Strouhal number and a higher drag coefficient. As explained in section 2.2.5, both coefficients are strongly related with wake width. According to Roshko [30], the wider the wake is, the higher the drag coefficient, and the lower the Strouhal number will be. It can be assumed then that a higher height-to-width ratio generates a wider wake (Figures 4.5 and 4.4).

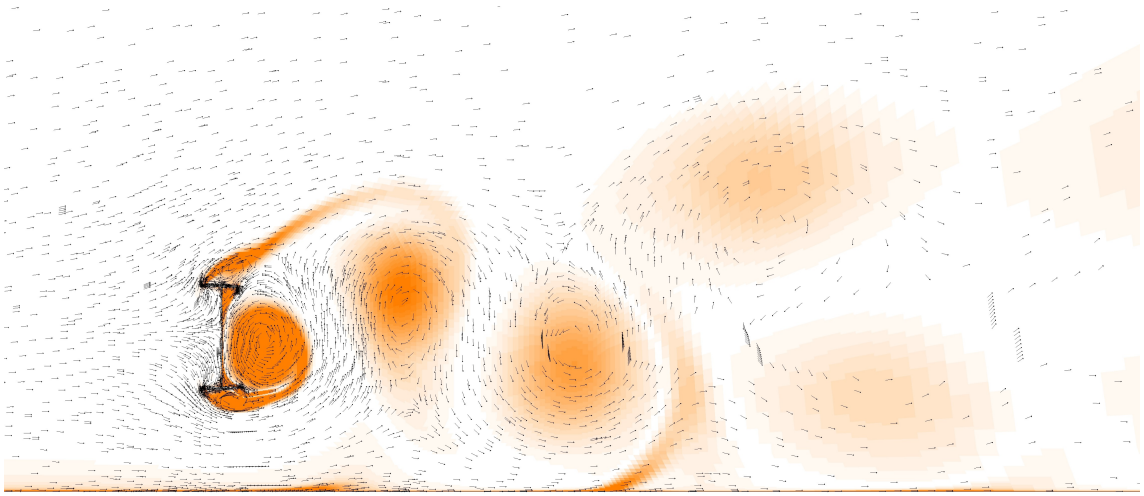

Figure 4.3: Vorticity contour for a particular moment of the simulation with $h = 3\,m$, $b = 0.9\,m$, $H = 3\,m$ and $U = 5\,m/s$. It can be seen how the central axis of the wake is displaced upwards due to the influence of the ground.

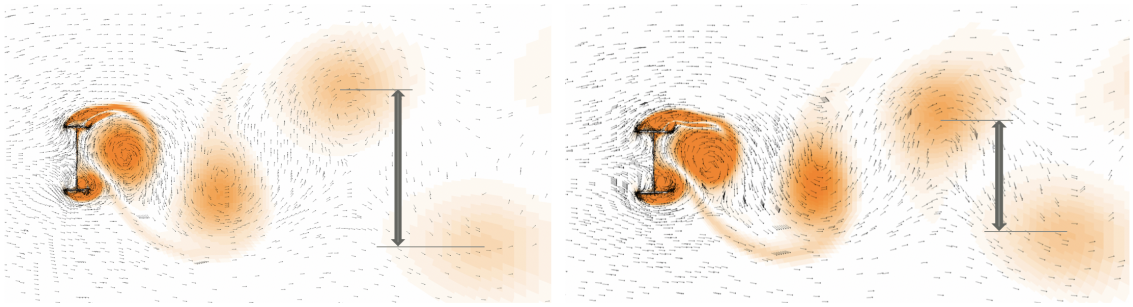

Figure 4.4: Vorticity contour at a particular moment of the single beam simulations in free flow, with $h = 3\,m$ (left) and $h = 2\,m$ (right). It can be observed how the wake size in proportion to beam's height changes.

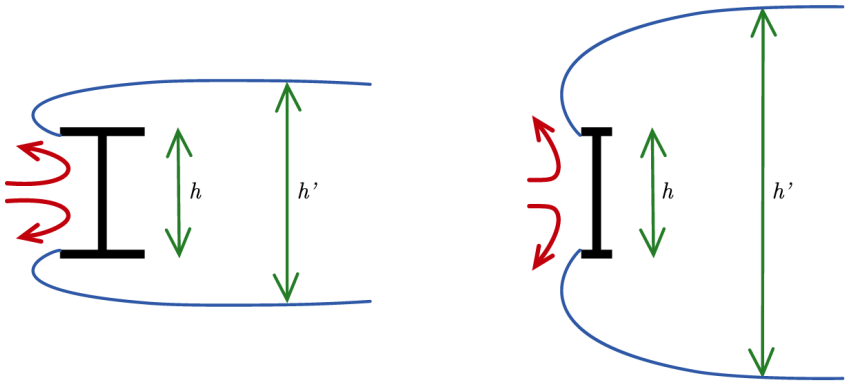

Figure 4.5: Possible explanation for the changes in the wake width with increasing height of the beam. Shorter flanges might change the scape angle of the flow.

Finally, the height of the bridge H increases both drag coefficient and Strouhal number. This effects can be related with the blockage effect present in wind-tunnel tests. If the walls of the tunnel are near to the shape tested, the fluid has more difficulties to surround the body and the pressure before the obstacle increases (Figure 4.6), giving results that differ from free flow observations. In this case, the ground is acting as a wall, increasing the pressure in the upwind zone. An increase of pressure explains the increase in the drag coefficient and Strouhal numbers.

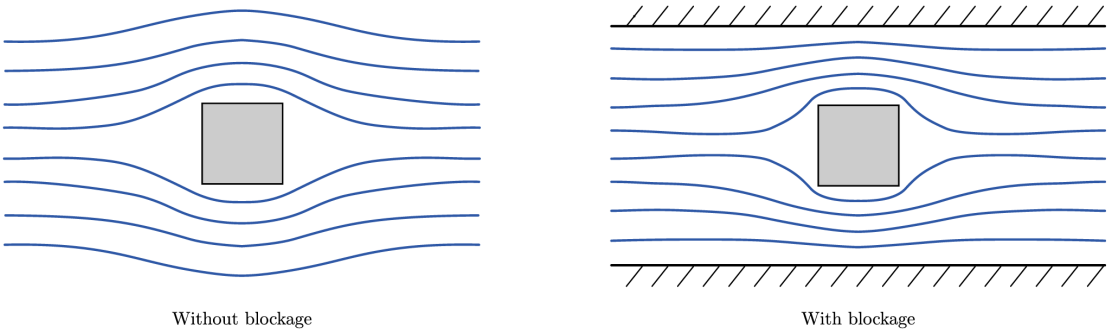

Figure 4.6: Changes in the flow due to the proximity of walls (blockage effect).

RMS values of drag and lift coefficient

The parameters representing the amplitude of oscillations of drag and lift forces are shown in Figure 4.7. Is is possible to see that the results with bridge heights $H = 3$ follow the same trends as the other simulations, but they still being different. Moreover, the blockage effect mentioned in the previous section appears again in this case.

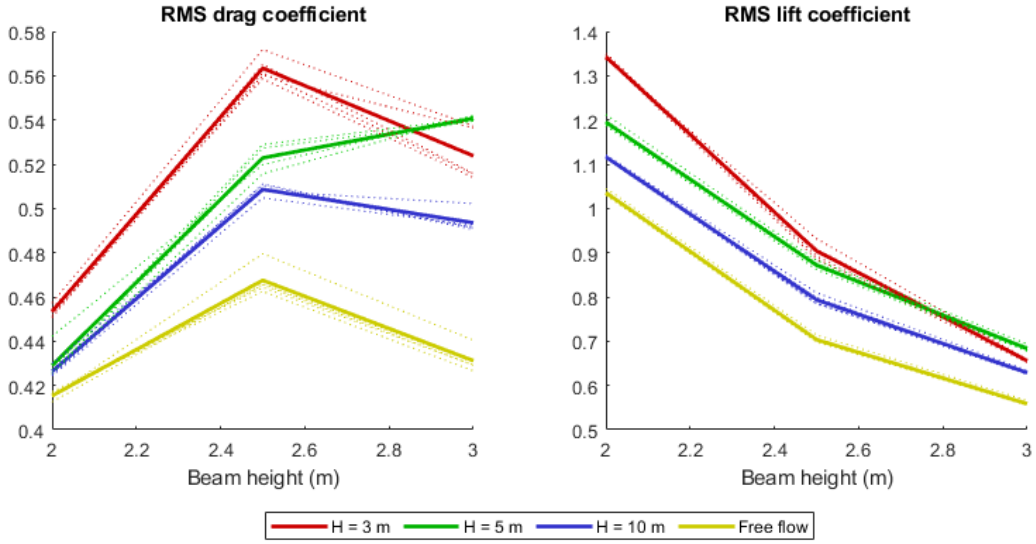

Figure 4.7: Root Mean Square (RMS) values of the drag and lift coefficients extracted from the simulations with one beam. The dotted lines represent the results for a particular wind speed, while the continuous lines are the average values from all the wind speeds.

The amplitude of the lift coefficient shows a great decrease when beam height increases. In order to calculate the lift coefficient, it is necessary to divide the lift force by the height of the beam, but the surface where the pressure can create lift forces is always the same. This means that the lift forces are similar for the different beam heights, but the lift coefficient changes because the changes in the reference dimensions.

About the amplitude of the drag coefficient, it can be observed a peak for simulations with an intermediate beam height ($h = 2.5\,m$). Both options, increase or decrease the beam height, would be good then to reduce the dynamic loads in the along-wind direction. However, it would be necessary to make more simulations, as three values is not enough to see clear trends in this case.

4.2 Situation 2: Double beam

When both of the beams are located in their final positions, the phenomenon turns much more complex. In Figure 4.8 shows the appearance of vortexes in the zone between beams. This creates a high kinetic energy region, which results into a low pressure zone.

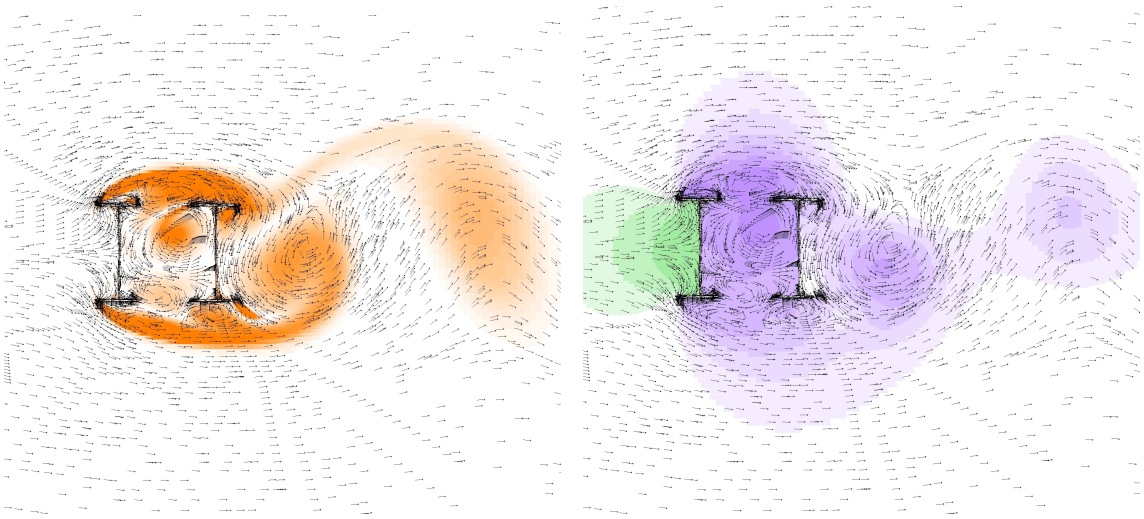

Figure 4.8: Vorticity field (left) and pressure field (right) for a simulations with two beams. Orange colors represent the vorticity, purple represents low pressure zones and green high pressure zones.

This situation can be divided into two different structural cases. A first case where both beams can move independently, and a second case where both beams are joined by steel elements, acting then as a single structure. Therefore, all the aerodynamic coefficients can be calculated for each beam independently and for both beams as a single body, giving three different values for each parameter.

4.2.1 Comparison between cases

Figure 4.9 shows the values of the principal coefficients obtained for the first two situations analysed. Note that, for the second situation, the results for each independent beam and for both beams joined are showed.

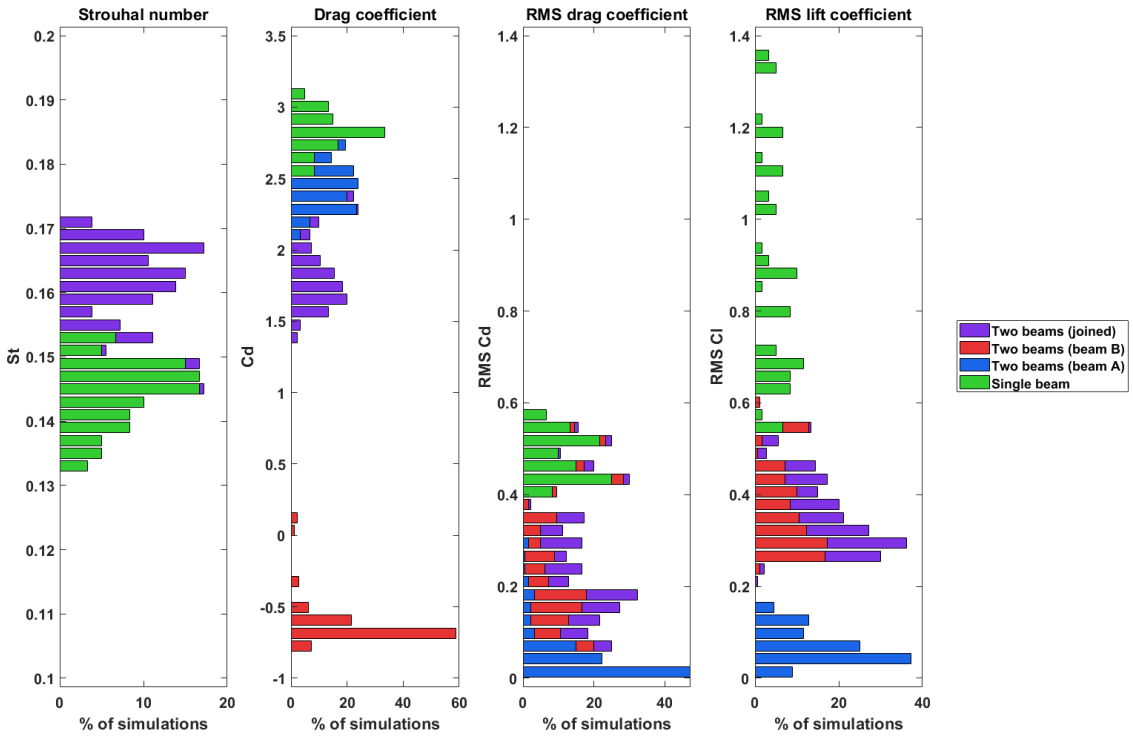

Figure 4.9: Distribution of the Strouhal number, drag coefficient and Root Mean Square values of the drag and lift coefficients for the different situations and structural configurations.

As it can be observed in the graph, the Strouhal number grows about a 10-15% from the first situation to the second situation, which implies a reduction of the critical velocity. About the mean drag coefficient, the second situation gives lower values than the single beam situation. It can also be seen that the downwind beam has a negative drag coefficient, generated by the low pressure zone between both bodies.

According to the work of Roshko [30], the variations in drag coefficient and Strouhal number indicate that the second simulation creates a thinner wake than the first one, increasing the frequency of vortex shedding but decreasing the wind loads on the shape.

Regarding the variations of the drag and lift coefficients, the two of them decrease when both beams are located in their final position, specially in the case of the lift coefficient. It can also be seen that the downwind beam is the one which receives the bigger dynamic actions, while the upwind one has almost no variations in the forces.

It is important to say that the amplitudes of the drag coefficient are in the same order of magnitude as the amplitudes of the lift coefficient. Despite vortex shedding predominant actions are in the cross-wind direction, very high and thin shapes amplify drag forces and decrease lift forces, making them comparable. Taking into account that the drag coefficient has twice the frequency as the lift coefficient (Section 2.4), the dynamic actions in the along-wind direction might be more dangerous for the structure than the ones in the cross-wing direction. Furthermore, the bending stiffness is much lower in the along-wind direction, leading to lower natural frequencies in the horizontal plane.

4.2.2 Upwind beam

As said in the previous section, the amplitudes of the drag and lift coefficient are very low for the first beam. That means that the dynamic effects induced by the vortex shedding phenomenon are not important in this case. However, the upwind beam absorbs all the drag coefficient, which might be important to calculate possible buffeting effects.

The drag coefficient is lower than in the first situation, but it stills being high. Again, it shows an increase when beam height increases (Figure 4.10), just as in the single beam situation. Probably, the most interesting thing is that the parameter decreases around a 10% when the distance between beams increases half a meter.

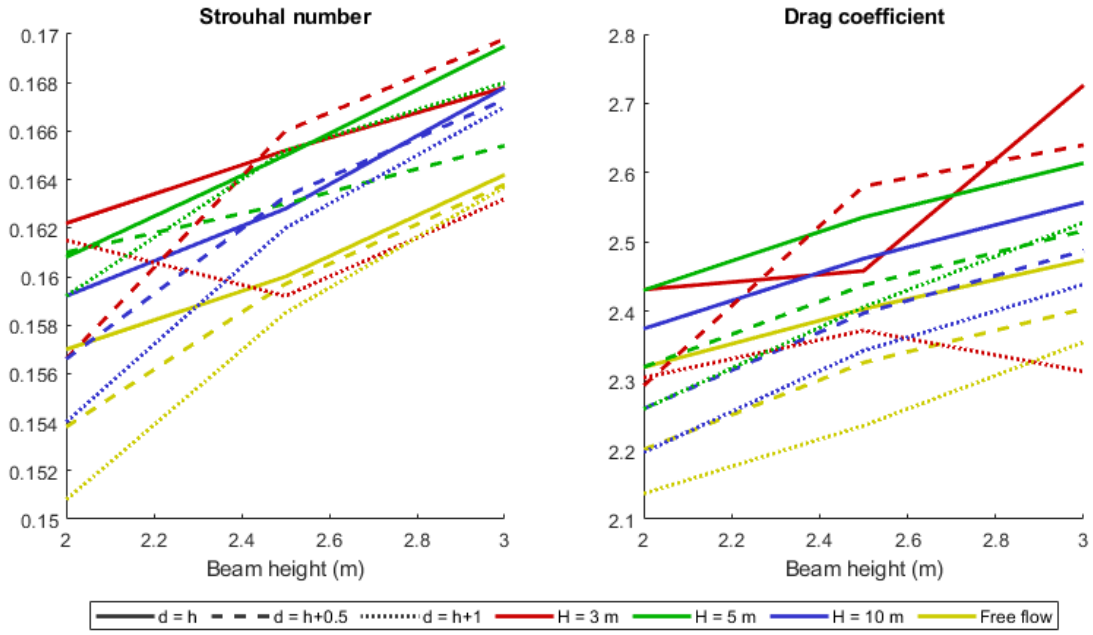

Figure 4.10: Values of the Strouhal number and drag coefficient for the upwind beam, extracted from the simulations with two beams.

Regarding the Strouhal number, unlike in the first situation, the parameter increases when the height of the beams increases. Thus, the frequency of vortex shedding stops being inversely related with the drag coefficient. Moreover, the coefficient also shows a small decrease when the distance between beams increases.

It is important to say that Strouhal number will be equal for all three structural cases, as is a property of the flow around the section and not an action on a specific body.

4.2.3 Downwind beam

In the case of the second beam, located in the downwind zone, the mean drag coefficient is not a problem. However, the oscillations in the drag and lift coefficients are much greater than in the first beam.

The first thing to notice is that both amplitudes are in the same range of values, going from 0.1 to 0.5 (Figure 4.11). This confirms that the dangerous actions induced by the vortex shedding are the ones in the along-wind direction, with double the frequency than lift oscillations.

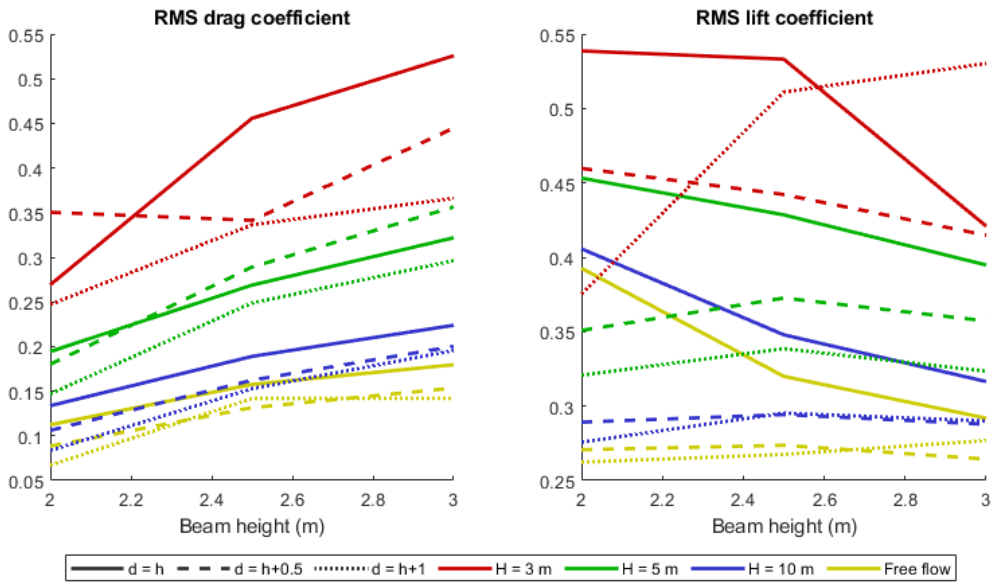

Figure 4.11: Root Mean Square (RMS) values of the drag and lift coefficients for the downwind beam, extracted from the simulations with two beams.

When beam's height increases, an increase in the amplitudes of the drag coefficient can be observed, following the same trend as the mean drag coefficient in the upwind beam. About the influence of the distance between beams, a slight reduction of the coefficient can be observed when beams' distance increases. However, it is not as significant as in the first beam.

Regarding the cross-wind amplitudes, their values decrease when beam's height increases, but only in cases when both beams are near. Furthermore, a significant reduction in the coefficient can be observed when beam' distance is increased.

4.2.4 Joined beams

When both beams are joined by the bracing, the structure takes most of the coefficients from the actions in one of the beams. On the one hand, the drag coefficient is very similar to the drag coefficient of the first beam, as the second one has a very low and negative drag. It follows then the same relations with the geometrical parameters explained before. On the other hand, the RMS values of the drag and lift coefficient are almost the same as in the second beam, since the first beam has really low oscillations in the forces.

By last, it is important to mention that, in this case, the torsional variations must be taken into account. The maximum values of the lift coefficient do not occur at the same time in both beams, there is a phase difference between them. These lift forces, now applied with some eccentricity respect to the centroid of the section, lead to a higher oscillation in the torsional forces than in the previous cases.

The RMS values of the moment coefficient are between 0.1 and 0.4. However, in the simulations with free flow conditions, the parameter is always around 0.1. This evidences that the main part of the torsional actions are caused by the influence of the ground, and not only the phase difference between the lift forces in both beams. About the influence of the distance between beams, no evident changes can be seen with variations in the geometrical parameter. A longer distance implies higher moments created by the lift forces, but it also changes the phase difference between the forces. Thus, it is difficult to find clear relations between this geometrical parameter and the results.

4.2.5 Overview

An overview of the influence of each geometrical parameter in the principal aerodynamic coefficients is shown in Table 4.1. As it can be observed, increasing the distance between beams leads to a decrease in almost all aerodynamic coefficients, so it seems to be the better option to reduce the vulnerability of the section to dynamic wind loads.

	St	Beam A			Beam B			Both beams joined		
		C_D	RMS_{C_D}	RMS_{C_L}	C_D	RMS_{C_D}	RMS_{C_L}	C_D	RMS_{C_D}	RMS_{C_L}
↑ h	↑	↑	=	↓	=	↑	↓	↑	↑	↓
↑ d	=	↓	↓	↓	↑	↓	↓	↓	↓	↓
↑ H	↓	↓	=	=	=	↓	↓	↓	↓	↓

Table 4.1: Influence of the variations of each geometrical parameter on the aerodynamic coefficients of the section. Small arrows represent maximum changes around 5-10%, while big arrows represent maximum changes of more than 10%. The bright yellow cells denote the parameters that have a significant values, while the white cells mark the negligible coefficients.

4.3 Situation 3: Closed section

The alternative case defined in situation 3 results in a completely different flow behaviour around the shape (Figure 4.12). The vortexes are formed farther from the section, and it can be seen how the low pressure zones act over a longer surface.

Structurally, this situation can only be created when both beams are joined and act as a single structure.

4.3.1 Comparison between cases

Figure 4.13 compares the overall results from all the simulations between the situation 2, with both beams joined, and situation 3.

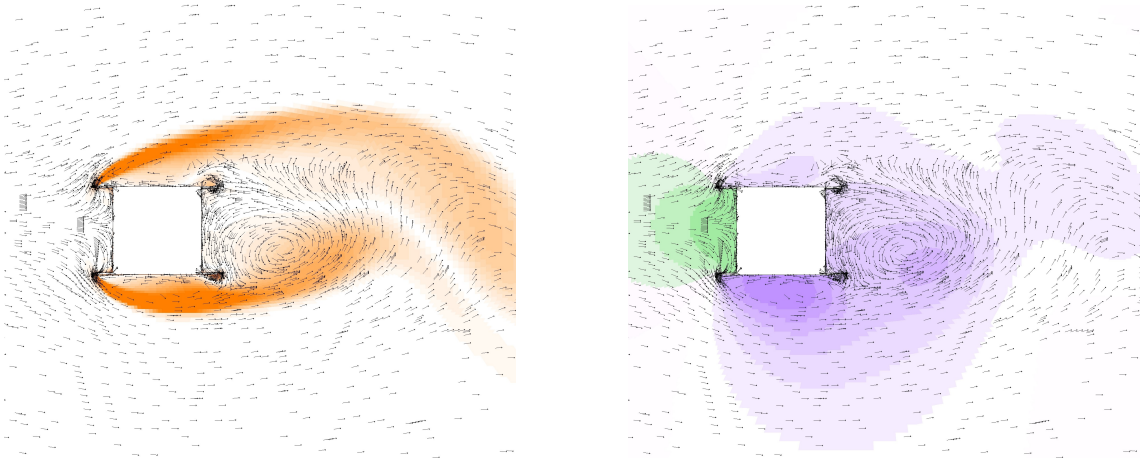

Figure 4.12: Vorticity field (left) and pressure field (right) for a simulations with two beams and isolated interior. Orange colors represent the vorticity, purple represents low pressure zones and green high pressure zones.

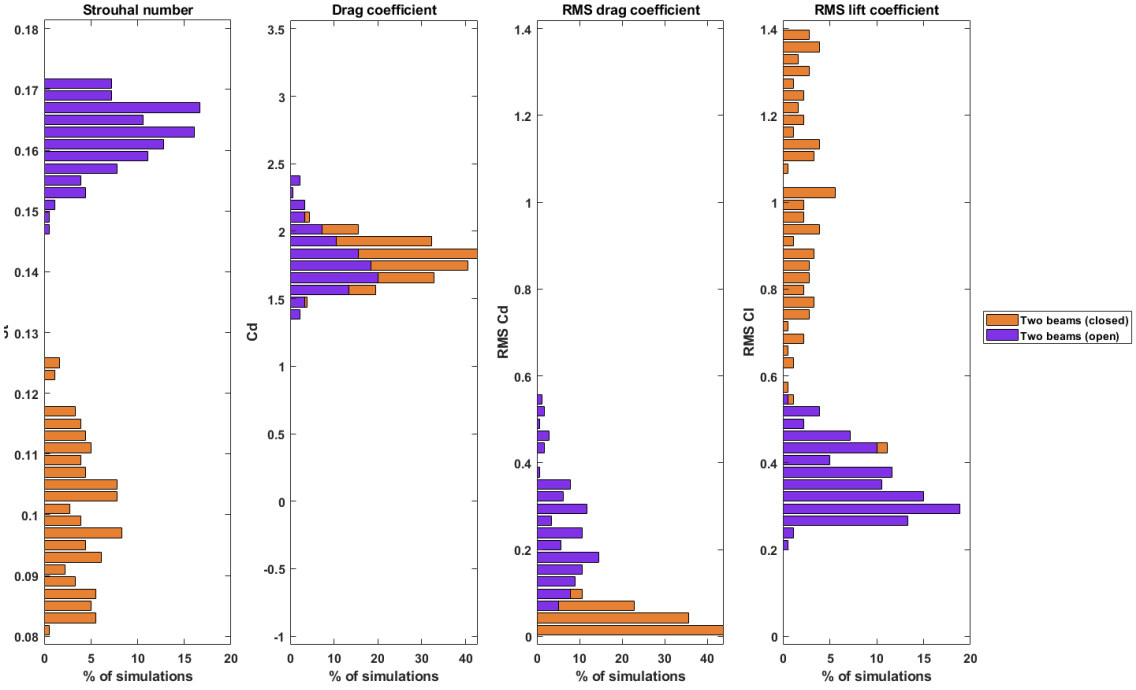

Figure 4.13: Distribution of the Strouhal number, drag coefficient and Root Mean Square values of the drag and lift coefficients with and without the the wooden/steel slabs isolating the space between beams.

The first thing to notice is that the Strouhal number decreases around a 50%. The lower the Strouhal number is, the higher will be the critical wind speed, making less probable to find resonance. Therefore, this drop in the coefficient is really useful to reduce the vulnerability of the bridge to dynamic wind effects.

Furthermore, the amplitudes of the drag coefficient also drop to almost zero values, reducing the effects of the wind even if the frequency of vortex shedding meets the natural frequency of the structure.

Regarding the lift coefficient, its amplitude grows considerably due to the increase in the lateral surface of the section. However, as said in previous sections, the principal risk comes from the along-wind direction forces, so the increase in the coefficient does not limit the utility of the alternative.

4.3.2 Influence of the parameters

The influence of each geometrical parameter on the final aerodynamic coefficients also differs from situation 2. In this case, the Strouhal number seems to be independent of the height of the bridge, but continues increasing when beam's height increases (Figure 4.14). Moreover, the distance between beams has a greater influence than in the previous situation. Increasing beams' distance, the Strouhal number decreases.

About the drag coefficient, same relations as before can be applied (Figure 4.14). However, the influence of the height of the bridge and the beam is slightly lower, while the distance between beams is more important to define this parameter.

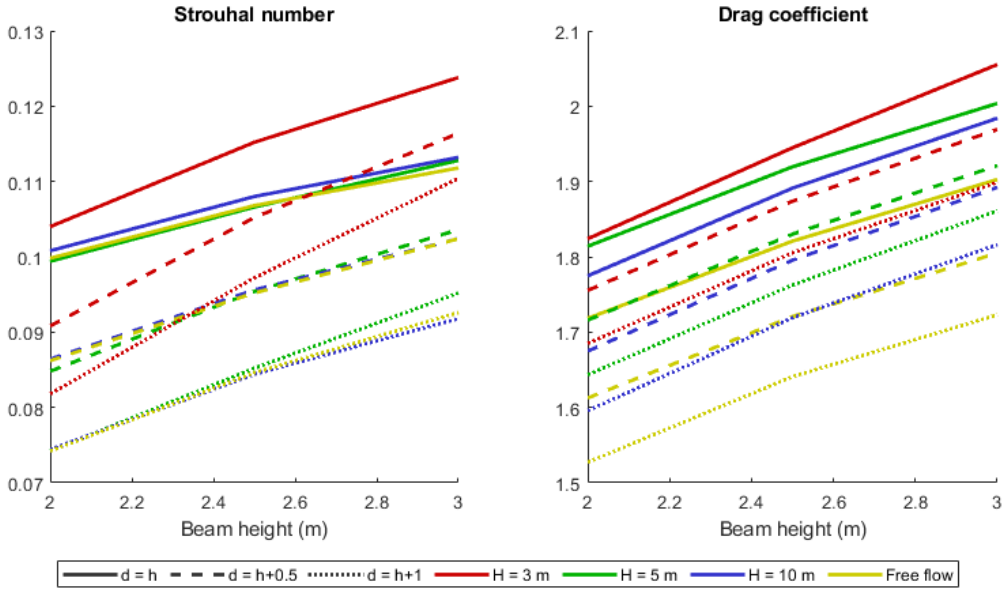

Figure 4.14: Values of the Strouhal number and drag coefficient extracted from the simulations with two beams with closed section.

Regarding the amplitudes of drag and lift coefficient, both parameters are highly influenced by the height of the bridge, increasing as the height decreases (Figure 4.15). Both coefficients grow slowly when the height of the section increases or the distance between beams decreases.

Table 4.2 shows an overview of all the relations between geometrical parameters and aerodynamic coefficients. It can be seen, that the solution of increasing beams' distance stills being favourable in this situation.

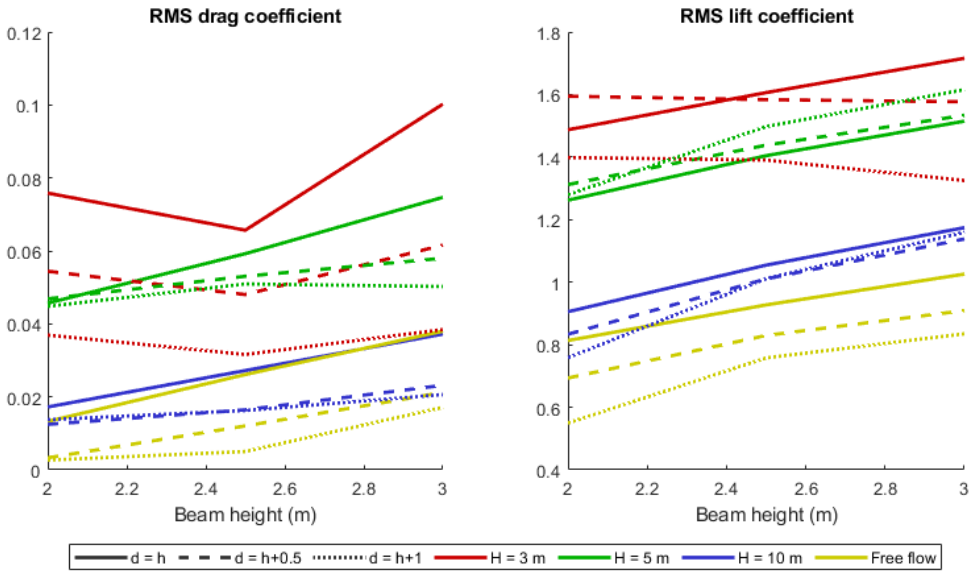

Figure 4.15: Root Mean Square (RMS) values of the drag and lift coefficients extracted from the simulations with two beams with closed section.

	St	C_D	RMS_{C_D}	RMS_{C_L}
↑ h	↑	↑	↑	↑
↑ d	↓	↓	↓	↓
↑ H	=	↓	↓	↓

Table 4.2: Influence of the variations of each geometrical parameter on the aerodynamic coefficients of the closed section. Small arrows represent maximum changes around 5-10%, while big arrows represent maximum changes of more than 10%. The bright yellow cells denote the parameters that have a significant values, and not near to zero.

Chapter 5

Banafjäl Bridge response

5.1 Introduction

The intention of the present chapter is to apply the results obtained in Chapter 4 to a particular case study, in order to analyse the structural response of a simple girder bridge to wind induced loads.

The bridge chosen for this analysis is the Banafjäl Bridge, a single lane railway bridge which forms part of The Bothnia Line. This particular bridge is specially convenient to analyse for several reasons. On the one hand, bridge drawings and data were available for the author, and on the other hand, the bridge has specially low amplitudes of vibration, which makes it more vulnerable to dynamic effects.

To calculate the response of the structure, the analytical methods proposed by Eurocode 1 [14] were applied, but the geometrical parameters were replaced by the ones calculated in the parametric study (see Appendix A). Regarding the properties of the solid, the only data needed are the natural frequencies and the mode shapes of the structure. It is important to say that the uncertainties in the results mentioned in Section 1.4 were not taken into account, and the aerodynamic coefficients were used without any security coefficient. Therefore, the estimated response of the structure inherits the uncertainties from the previous sections, being possible only to estimate –and not determine– the final response. In order to have more reliable results, it would be necessary to make wind-tunnel tests to validate the computational results.

The analysis of a case study is of special importance for the project. First, because it gives an example of application of the results and conclusions reached in previous sections. Second, to give an estimation of the response's magnitude in this type of bridges. Simple girder bridges with the analysed section usually have their parameters in the same range of values, so their responses might be comparable. By last, the case study is a good opportunity to assess different alternatives in the design to reduce the vulnerability of the bridge.

In conclusion, the response of Banafjäl Bridge to wind induced vibrations is analysed in this chapter. In order to do so, it was necessary to make Finite Element Method (FEM) models to calculate the natural frequencies and modes of vibration of the bridge. After that, the analytical methods from Eurocode 1 were used with the aerodynamic coefficients obtained in this report.

5.2 The Banafjäl Bridge

The Banafjäl Bridge is one of the infrastructures forming the so-called Bothnia Line. This higher-speed railway track connects Höga Kusten Airport with Umeå, and is part of a bigger project: a railway corridor connecting southern Sweden with southern Finland (Figure 5.1). The corridor goes along the Baltic sea coast and it is prepared for trains travelling up to 300 km/h.

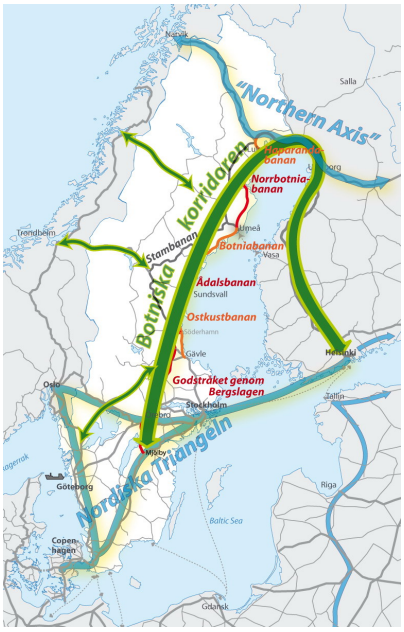

Figure 5.1: Bothnian corridor project. SOURCE: Midway Alignment [25].

In particular, Banafjäl bridge is located 15 km east from Örnsköldsvik, near the lake Lill-Mosjön (Figure 5.2). The bridge crosses the small river Banafjälsån while travelling parallel to the E4 highway.

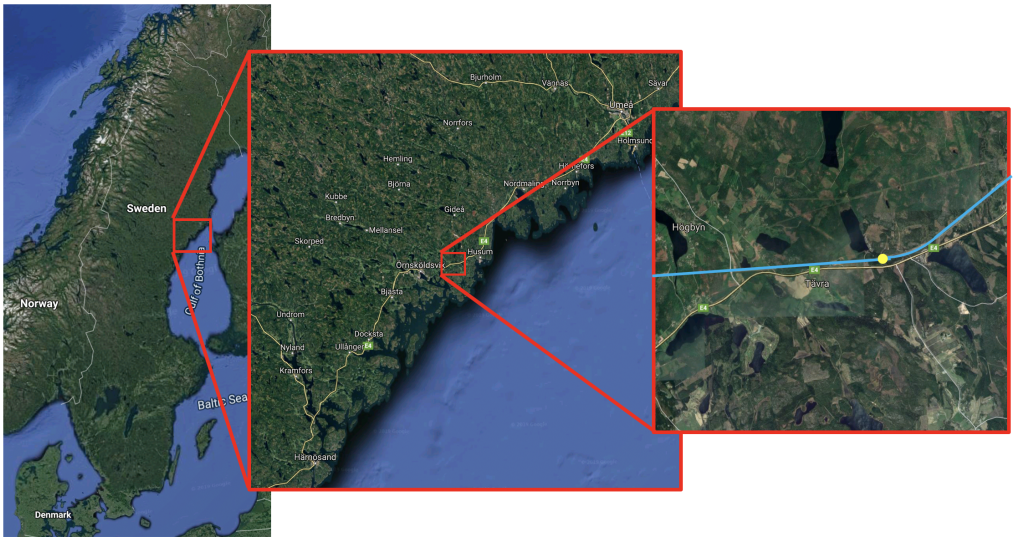

Figure 5.2: Location of Banafjal Bridge. The blue line represents the Bothnia Line, while the yellow dot marks the location of the bridge.

5.2.1 Geometrical characteristics

The Banafjäl Bridge is a 42 metres long composite bridge formed by two I beams with a concrete slab over them (Figure 5.3). The distance between the ground and the lower part of the structure is around seven meters, being a little bit smaller in the surroundings of the supports.

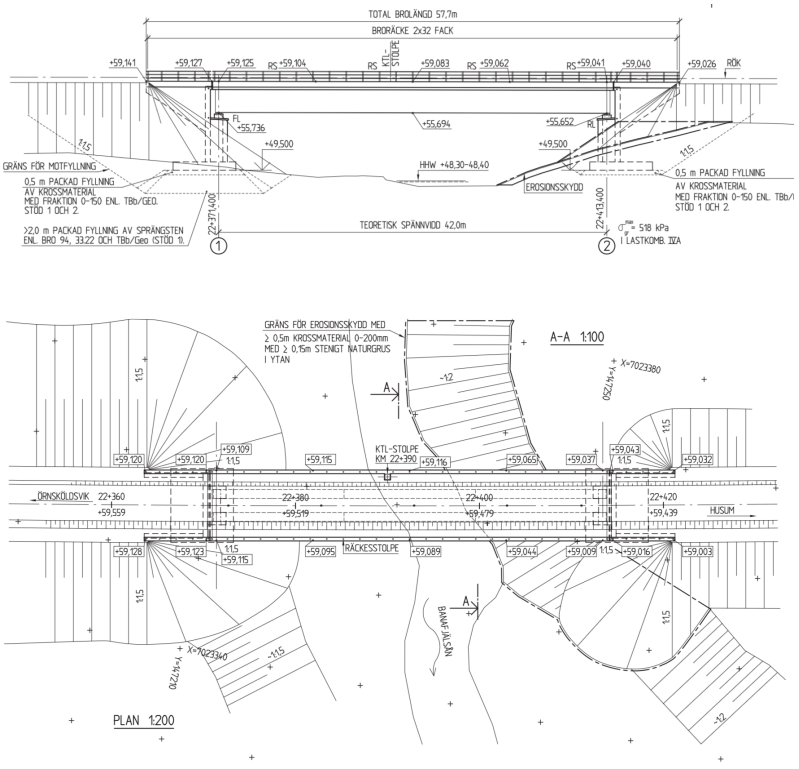

Figure 5.3: General views of Banafjäl Bridge. SOURCE: Skanska drawings.

Regarding the section, the steel beams are $h = 2.5\,m$ height with flanges $b = 0.9\,m$ width (Figure 5.4). The distance between beams is $d = 2.5\,m$. Thus, the geometrical dimensions are in the range tested in the parametric study. The flanges of the beams are made of steel S460M, while the web is made of steel S420M.

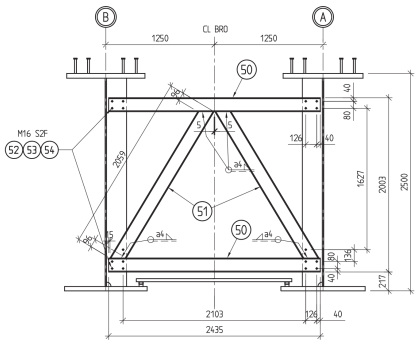

Figure 5.4: Cross-section of Banafjäl Bridge without the concrete slab. SOURCE: Skanska drawings.

5.3 Method

As said in the introduction, the only data needed from the structure is its natural frequencies and mode shapes. In order to obtain them, a Finite Element Method (FEM) model was made with the software Ansys-Mechanical. The geometry introduced in the model was generated with the software Ansys-SpaceClaim. In this case, none of the processes was automatized, as the amount of models to analyse is not big.

It is important to mention that only two situations were analysed with the FEM models: a single beam and two beams joined by the bracing. The second situation, when both beams are placed but they are not joined yet, behaves structurally like when only one beam is placed. About the situation with wooden or steel plates closing the section, the plates were assumed to be non-structural and very light, so the natural frequencies are the same as in the case with two beams joined by the bracing.

5.3.1 FEM models

All the elements in the structure are flat steel pieces, so shell elements were used to represent them in the model. The bracing was also modelled with shell elements according to the bridge drawings.

Regarding the spatial discretization, the mesh was created with the automatic mesh generator from the software, resulting in 21000 elements for the single beam model and 26000 elements for the double beam model.

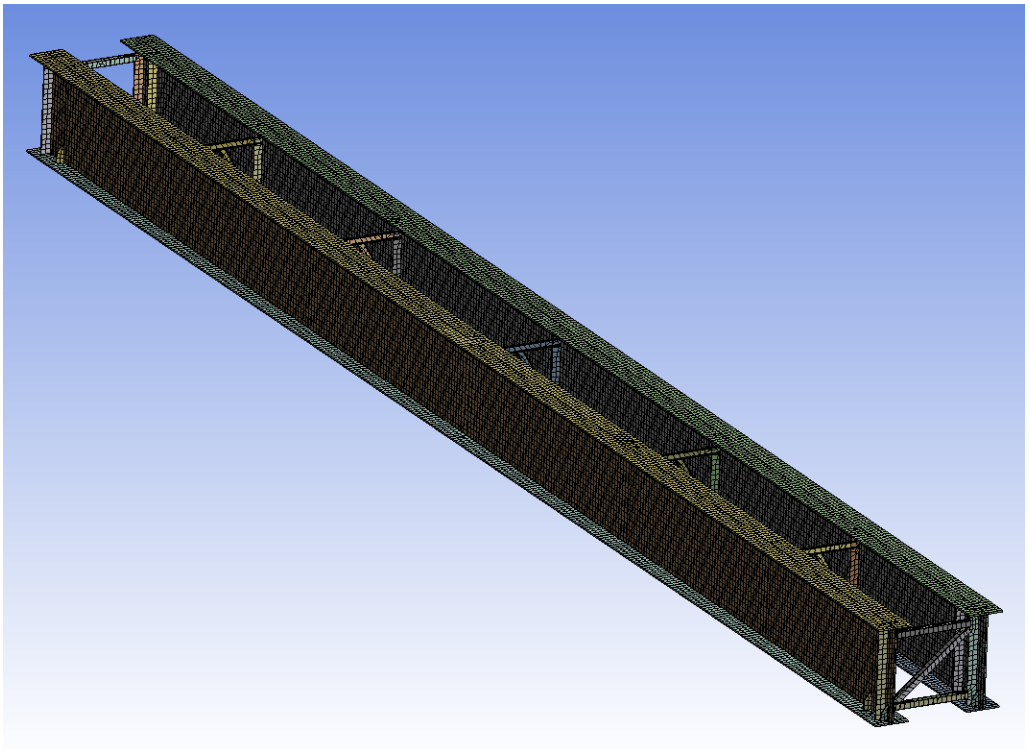

Figure 5.5: Mesh of the model with two beams joined by the bracing.

Boundary conditions

The boundary conditions were different in each case. The beams are usually sustained by a circular piece that allows the rotation in one direction but prevents the displacements. An elastic piece allows also the rotation in the other two directions (Figure 5.6). Furthermore, the connection between the mentioned piece and the beam can allow particular displacements to permit temperature deformations.

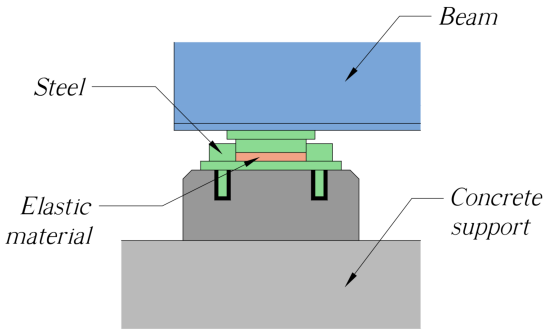

Figure 5.6: Supports detail without temperature deformations allowance.

In the case of the single beam model, a zero-displacement support was set in lower flange of one of the extremes, while the other extreme allowed the deformation in the longitudinal direction. However, this disposition permits the rotations, allowing the beam to overturn laterally. In reality, as the beams have a height section, it is necessary to have a provisional system to prevent the overturn when they are not held to the other beam. In the worst case scenario for the dynamic behaviour of the structure, both pieces are sustained by fastenings on the supports, allowing free displacements along the deck. Thus, a new boundary condition was added in the extremes of the top flanges, preventing the lateral displacement.

Regarding the double beam model, the conditions in the top flanges are no longer needed, since the structure has four supports and the rotation is impeded. However, the second beam has new degrees of freedom to allow transversal temperature deformations.

Figure 5.7 shows the displacements allowed in each of the supports. Note that the vertical displacement –perpendicular to the image– is always impeded. The longitudinal displacement in the bottom-left support is not needed for temperature deformations. However, small displacements might be allowed by small imperfections in the support, permitting the rotation of the whole structure in this extreme of the bridge.

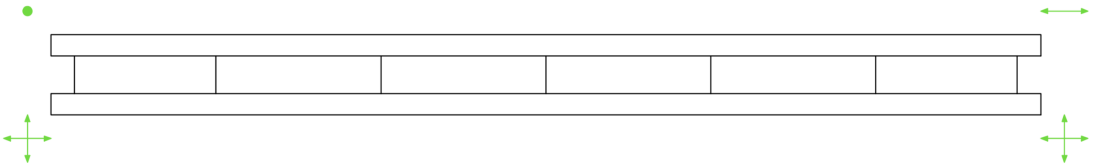

Figure 5.7: Upper view of the steel structure of the bridge with the degrees of freedom of each support as implemented in the model.

5.3.2 Alternatives

Four different alternatives were also tested in case the bridge needed modifications to reduce its vulnerability to wind effects:

- **Alternative 1:** Increase beams' height from $h = 2.5\,m$ to $h = 2.75\,m$. A higher section implies bigger drag forces, but also increases the natural frequencies of the beams' vertical bending modes. In this case, the upper level of the bridge is conditioned by the railway track, so the increase in the section was added in the lower part, reducing bridge's height to $H = 6.75\,m$.

- **Alternative 2:** Increase beams' width from $b = 0.9\,m$ to $b = 1\,m$. In this case, both vertical and horizontal frequencies of vibration are expected to grow.

- **Alternative 3:** Increase beams' distance from $d = 2.5\,m$ to $d = 2.75\,m$. As observed in Chapter 4, this variation reduces wind effects on the bridge.

- **Alternative 4:** No modifications in the geometry of the beams, but placement of wooden/steel plates to close the section, as explained in Section 3.1.1.

5.3.3 Analytical analysis

The analysis of Banafjäl's response was made with the analytical methods proposed in Eurocode 1, already explained in Section 2.6.

For the along-wind response of the structure, the second procedure –originally proposed by Dyrbye *et al.* [12]– was used. It is important to mention that the analytical method aims to check the structure's response to a particular wind, which is associated with a specific return period. As the construction stages analysed in this report are provisional, the analysis will be made with different wind speeds to see where are the limits of the structure. Thus, the maximum wind speed that can be supported by the structure without any plastic behaviour has been calculated.

Regarding the vortex shedding response, the first method proposed by the normative was used, as it is more appropriate for flexible steel structures. Even though this method was initially designed to analyse the cross-wind response, it was adapted to check also the along-wind response for reasons already explained in Chapter 4. The frequency of vortex shedding was in this case twice the one for cross-wind vibrations, and the vibrations in the horizontal direction were assumed to be capable of synchronizing the vortex shedding phenomenon along the structure.

Only the first bending mode of vibration was analysed. Eurocode 1 methods are not valid for modes with changing sign or torsional modes. Besides, the first bending moment showed to be the one with the lowest frequency, being more vulnerable to wind loads.

The aerodynamic parameters were extracted by interpolations with the results shown in appendix A. Note that, in the case of the second alternative, beams' width changes but there are no results with different flanges' size. In this case, as the phenomenon is shape –and not size– dependent, the height of the beams and the bridge was reduced in proportion to calculate the aerodynamic parameters.

5.4 Results and discussion

5.4.1 Mode shapes

The mode shapes are the same in all 5 study cases with small variations in the frequencies of vibration. Thus, only the modes of the original design of Banafjäl Bridge are shown in the following images. It is important to mention, that Alternative 4 will have always the same mode shapes and frequencies than the original design, as the plates were assumed to be light and without influence in the structural behaviour of the bridge. In a similar way, Alternative 3 will have the same frequencies as the original design when analysing only one beam, as each individual beam has the same dimensions.

Single beam

The first mode of vibration for the single beam is the horizontal bending moment (Figure 5.8), as it could be expected considering the low moment of inertia in this direction. The shape proved to be sinusoidal, being possible then to use the simplified formulas provided by Eurocode 1.

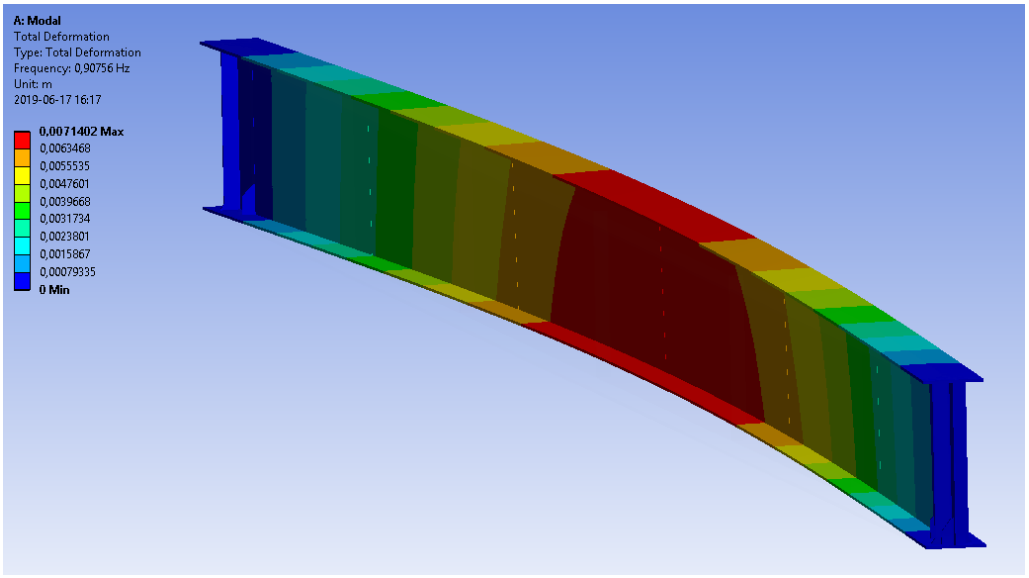

Figure 5.8: First mode of vibration of one of Banafjäl's beams. The colors represent the total displacement.

First mode of vibration (single beam)				
Banafjäl	Alternative 1	Alternative 2	Alternative 3	Alternative 4
0.9076 Hz	0.8894 Hz	1.0286 Hz	0.9076 Hz	0.9076 Hz

Table 5.1: Natural frequencies of one of Banafjäl's beams for its first mode of vibration and the different alternatives.

Regarding the frequencies, Table 5.1 shows the vibration frequencies of the first mode depending on the variations in the design. It can be observed that the first alternative slightly decreases the natural frequency, while the second one increases it. As the mode is horizontal, an increase in beams' height does not augment the moment of inertia but adds mass to the system, explaining

the slight decrease in the frequency. Regarding the second alternative, an increase in beams' width directly augments the bending stiffness of the beam, rising also the natural frequency.

The second mode, which corresponds to the torsional vibration, has slightly higher natural frequencies (Figure 5.9). Table 5.2 shows the natural frequencies for the different alternatives, showing the same influences than in the first mode.

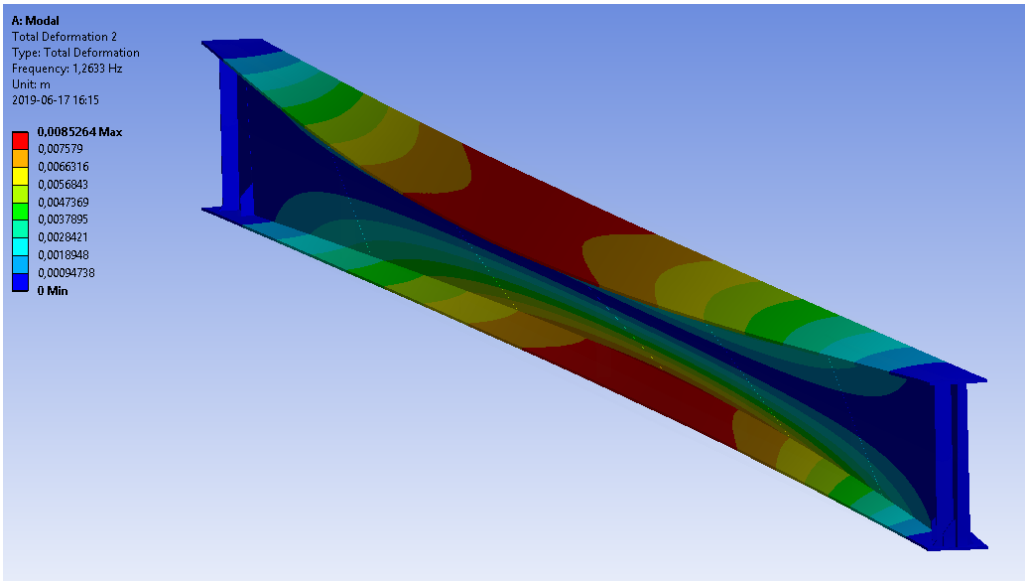

Figure 5.9: Second mode of vibration of one of Banafjäl's beams. The colors represent the total displacement.

Second mode of vibration (single beam)				
Banafjäl	Alternative 1	Alternative 2	Alternative 3	Alternative 4
1.2633 Hz	1.2218 Hz	1.3633 Hz	1.2633 Hz	1.2633 Hz

Table 5.2: Natural frequencies of one of Banafjäl's beams for its second mode of vibration and the different alternatives.

The third mode is the second horizontal bending mode. However, its frequency is around $n = 3.5 - 4\,Hz$, which is out of the range for vortex shedding evaluation. These frequencies need winds with $U > 30\,m/s$ to find resonance. Regarding the first vertical bending moment, its frequencies are around $n = 5\,Hz$.

Two beams joined

In the structural situation when both beams are joined by the bracing, the first mode of vibration is again the horizontal bending mode (Figure 5.10).

About the frequencies, it can be observed that they are quite similar to the ones obtained for the single beam (Table 5.3). This could mean that each beam bends in the same way as before, deforming the bracing to adapt it to the mode shape.

The second mode of vibration is in this case the second horizontal bending moment, with natural frequencies around $n = 3.5\,Hz$.

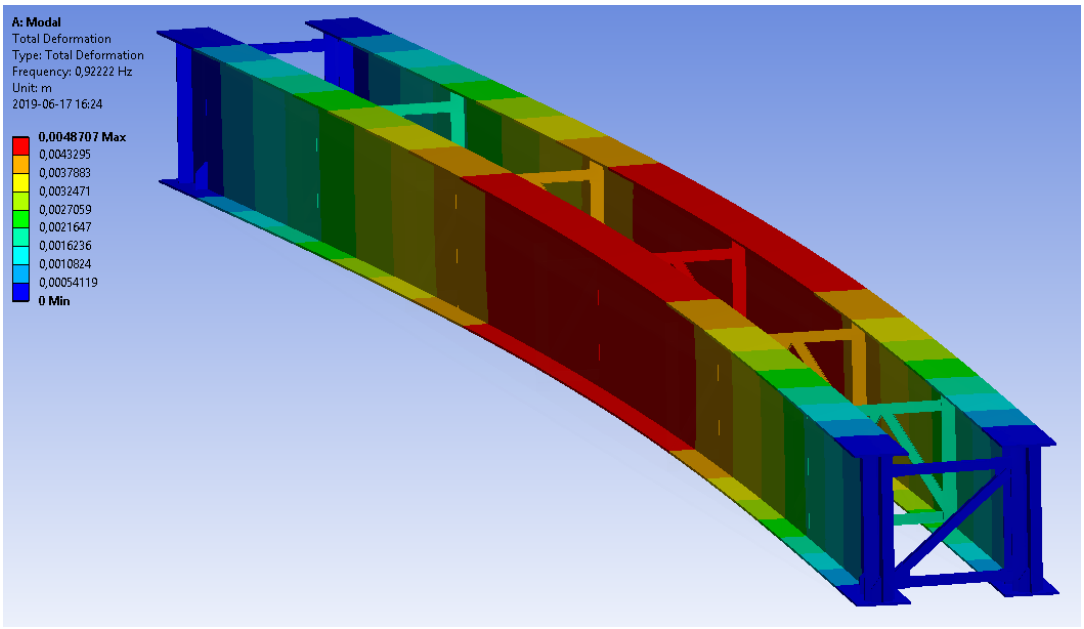

Figure 5.10: First mode of vibration of Banafjäl's steel structure. The colors represent the total displacement.

First mode of vibration (double beam)				
Banafjäl	Alternative 1	Alternative 2	Alternative 3	Alternative 4
0.9222 Hz	0.901 Hz	1.0385 Hz	0.9309 Hz	0.9222 Hz

Table 5.3: Natural frequencies of Banafjäl's steel structure for its first mode of vibration and the different alternatives.

5.4.2 Buffeting response

As said in Section 5.3.3, an inverse procedure was taken to calculate buffeting response. Instead of checking the resistance of the structure with a given wind speed, several wind speeds were tested to find the maximum flow velocity that does not cause plastic effects. If this speed is surpassed during a construction stage, plastic effects would appear, generating residual stresses in the beam.

Each construction stage has different durations, so different peak wind speeds can be expected. When designing the construction plan of the bridge, it will be necessary then to have sufficiently short times in each construction stage to ensure that the maximum wind speed will not be surpassed.

Figure 5.11 shows the maximum stresses in the steel section depending on the incident wind speed. It is important to mention that, in the situation with both beams joined by the bracing, the generated moment was divided between both beams. As seen in the mode shapes, each beam bends independently, deforming the bracing. Thus, geometry cannot be treated as a single section with a higher moment of inertia.

Note that only one value was given for the situation with two beams without connections. The values showed are those corresponding to the upwind beam, since the down wind has almost no drag force (see Section 4.2).

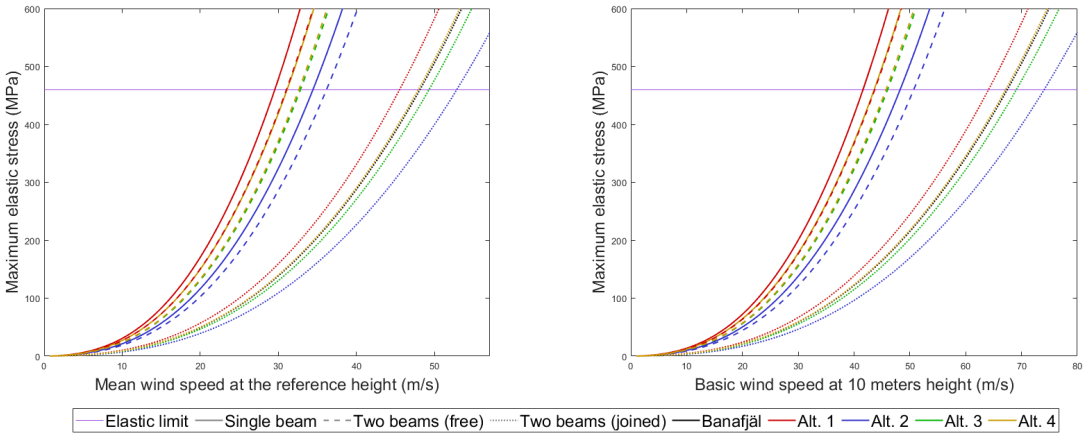

Figure 5.11: Maximum stresses in the steel according to Eurocode 1 methods, depending on the mean wind speed (at the height of the bridge) and on the basic wind speed (mean wind speed at 10 meters height).

	Maximum wind speed with elastic behaviour (m/s)				
	Banafjäl	Alt. 1	Alt. 2	Alt. 3	Alt. 4
Single beam	31.1	29.5	34.4	31.1	31.1
Two beams (free)	32.6	31.1	36.1	32.8	32.6
Two beams (joined)	48.11	45.5	52.8	49.5	47.9

Table 5.4: Maximum wind speeds supported by the structure without plastic effects. Each situation has different colour levels, as the differences between the last case and the previous two cases is considerable.

As it can be seen, when both beams are joined the generated stresses are lower than in other cases, since the actions are divided between both beams. This effect can also be observed in Table 5.4, which shows the maximum wind speeds without plasticity.

The results for the single beam situation and for the double beam without bracing are very similar. The frequencies of vibration are the same in these cases and there is only a slight decrease in the drag coefficient for the second case. Nevertheless, when the bracing has been built, the stresses reduce and the maximum flow speed tolerated by the structure increases considerably.

Regarding each alternative, increase beams' width (Alt. 2) seems to be the most beneficial action, as the horizontal bending stiffness is directly increased. Increasing beams' height (Alt. 1), however, shows opposite results. An increase in section's height implies a bigger drag, and no increase in the horizontal bending stiffness, explaining the results.

About the last two alternatives, both have a low influence in the buffeting phenomenon. Increasing beams' distance (Alt. 3) slightly improves the situation when the bracing has been built. However, closing the space between both beams (Alt. 4) has no influence at all.

Overall, it can be confirmed that buffeting effects occur with higher wind speeds than vortex shedding effects. As said before, the time between the placement of the beams and the construction of the bracing is not long, so it is difficult to have around 30 m/s of wind speed. Regarding the third situation, winds above 40 m/s are not common, so the bridge seems secure considering buffeting effects.

5.4.3 Vortex shedding response

Four different parameters were chosen to be representative to evaluate vortex shedding response: the critical wind velocity where the frequency of vortex shedding meets the natural frequency of the structure, the maximum stress the steel supports due to the vibrations, the maximum amplitude of vibration and the maximum acceleration at any point of the bridge.

The structure's response for the different situations and alternatives is shown in Table 5.5. It is important to mention that, for the case with both beams joined, it was assumed that each beam takes half the actions. As explained before, the mode shape shows that the beams deform the bracing, moving in the same way as when the holdings were not built yet. Thus, considering a single moment of inertia with both beams would lead to the underestimation of the stresses.

The results for the two beam situation, before the construction of the bracing, are shown for the downwind beam. As explained in Section 4.2, the effects on the upwind beam are always lower than in the downwind beam.

		Vortex shedding response				
		Banafjäl	Alt. 1	Alt. 2	Alt. 3	Alt. 4
Single beam	Critical wind speed (m/s)	7.7	8.5	8.7	7.7	7.7
	Max stress (Mpa)	29.8	39.5	31.2	29.8	29.8
	Max displacement (mm)	60	80	57	60	60
	Max acceleration (m/s2)	1.95	2.49	2.36	1.95	1.95
Two beams (free)	Critical wind speed (m/s)	6.9	7.3	7.9	6.9	6.9
	Max stress (Mpa)	10.9	14.8	11.7	11	10.9
	Max displacement (mm)	22	30	21	22	22
	Max acceleration (m/s2)	0.71	0.93	0.88	0.72	0.71
Two beams (joined)	Critical wind speed (m/s)	7.0	7.4	8.0	7.1	10.3
	Max stress (Mpa)	12.9	16.7	14.1	12.1	3.6
	Max displacement (mm)	25	33	25	23	7
	Max acceleration (m/s2)	0.84	1.05	1.07	0.79	0.24

Table 5.5: Response of Banafjäl Bridge to vortex shedding for the different situations and alternatives.

The first thing that can be noticed is that the critical wind speeds are not very high, which implies that the actions and final stresses won't be high as well. The higher the wind speed is, the higher the forces are. Two times more wind velocity creates four times bigger actions. Thus, if the resonance occurs with moderate speeds, the final stresses are considerably lower.

The most dangerous effects caused by vortex shedding occur when only one beam is exposed to the flow. Nevertheless, as said before, this construction stage does not last too long. Usually, the placement of the beams takes one or two days, including the construction of the bracing.

Therefore, it would be recommendable to avoid to place the beams during a windy day. The critical velocities are in this case likely to happen, and resonance could cause big accelerations in the beam, leading to construction accidents.

After the bracing is done, the only effects left affect the discomfort in the construction, but do not seem to be dangerous for the stability of the bridge. Accelerations around $a_{max} = 1\, m/s$ are not very big, but can cause discomfort in the workers.

Regarding the influence of the different alternatives, increasing the height of the beams (Alt. 1) or their width (Alt. 2) slightly increases the critical wind speed and the effects. About increasing beams' distance (Alt. 3), no evident effects can be observed, so it would be necessary to increase it more to appreciate the effects.

The last alternative, closing the space between both beams, shows a clear improvement in the behaviour of the section. The critical wind speed increases, but the effects of the wind decrease. This alternative cannot improve the vulnerability before the bracing is done. However, the last stage lasts longer, so it is probably the most important one. Furthermore, there is no need to modify the project in this case, only the construction procedure, since the geometry of the beams still the same as in the original design.

In conclusion, Banafjäl Bridge shows a good behaviour regarding vortex shedding effects. Its specially low frequencies, around $n = 1\ Hz$, bring on the resonance with moderate wind speeds, where the effects are not very strong. In any case, closing the section with steel or wooden plates improves considerably the vulnerability of the bridge, reducing even more the risk.

However, similar simple girder bridges can easily have more problems with the vortex shedding phenomenon. For example, if the bracing stiffness was bigger, both beams would behave more as a single section, increasing the bending stiffness and the natural frequencies of vibration.

As an example, the calculations were made again assuming frequencies of vibration two times higher than the original ones, representing a stiffer bracing. Table 5.6 shows the response obtained.

		Vortex shedding response (double frequencies)				
		Banafjäl	Alt. 1	Alt. 2	Alt. 3	Alt. 4
Two beams (joined)	Critical wind speed (m/s)	14.0	14.9	16.0	14.2	20.6
	Max stress (Mpa)	51.5	66.5	56.5	48.4	14.5
	Max displacement (m)	25	33	25	23	7
	Max acceleration (m/s2)	3.38	4.19	4.28	3.17	0.95

Table 5.6: Response of Banafjäl Bridge to vortex shedding when both beams are joined, assuming that the natural frequencies are twice the ones extracted from the FEM model.

As it can be observed, the critical wind speeds grow considerably, leading to higher stresses. However, these stresses still being far from the elastic limit of the material. In any case, the accelerations also show a great increase, from $a_{max} = 1\ m/s$ to $a_{max} = 4\ m/s$ approximately. Accelerations of this magnitude create a strong discomfort, and can be dangerous for the workers. It would be recommendable then to stop the constructions when there are wind speeds near the critical flow velocity.

In this case, the effects of increasing beams' distance can be observed, with a slight reduction in wind effects and an increase in the critical velocity. However, the most effective alternative is again the disposition of plates to close the section. Alternative 4 shows a strong increase in the critical wind speed and divides by three or four wind effects.

Chapter 6

Conclusions and further research

6.1 Conclusions

The conclusions of the present report can be divided in two sections: the influence of the geometry in the flow and the structural response of the structure. The first one corresponds to the ideas extracted from the parametric study, while the second one refers to the structural responses calculated with the analytical methods from Eurocode 1.

The conclusions about the influence of section's geometry on the flow can be summarized in the following points:

- **Vortex shedding effects are more important in the along-wind direction with these types of sections.** The high height-to-width ratio of the beams reduces the cross-wind effects and amplifies the along-wind ones. Furthermore, the beams have less bending stiffness in the direction of the flow, resulting in lower frequencies of vibration and more vulnerability to dynamic effects.

- **Wind actions decrease when both beams are in their final location.** The actions on a single beam exposed to the flow showed to be considerably larger than when both beams are placed.

- **Buffeting effects are stronger on the upwind beam, while vortex shedding effects act on the downwind beam.** In construction stages where there is only one beam or there are two beams connected by the bracing, both phenomenons affect both beams.

- **Increasing the distance between beams is a good method to reduce wind effects.** Changing this distance does not reduce bridge's strength, but reduces the amplitudes of vibration of both drag and lift coefficients.

- **Placing wooden or steel plates isolating the space between the beams leads to a substantial decrease in along-wind effects.** This simple construction procedure decreases the Strouhal number around a 50%, and reduces also the amplitudes of vibration of the drag coefficient, which were the most problematic ones.

Regarding the structure's response to wind effects, and in particular Banafjäl Bridge response, the following conclusions can be extracted:

- **The most vulnerable stage is the one when only one beam is in its final location.** However, this situation does not last too long, as the placement of the second beam and the construction of the bracing can be done in one or two days.
- **Effects of buffeting can be dangerous with wind speeds above 25-30 m/s.** With these wind speeds, the steel can reach its elastic limit due to the vibrations of the structure. When bracing is already built, wind speeds above 40-45 m/s are necessary to have the same effects.
- **Increasing beams' height aggravates buffeting effects.** The increase in area perpendicular to the flow results in an increase on the stresses.
- **Increasing beams' width decreases buffeting response.** This modification increases the along-wind bending strength and the natural frequencies of vibration, reducing structure's vulnerability.
- **Vortex shedding effects are lower but more frequent than buffeting effects.** The resonance occurs with wind speeds between 5 and 15 m/s, and the generated stresses are far from the elastic limit of the steel. However, high accelerations can be found, reducing workers' safety and comfort.
- **Vortex shedding effects are low in the case of Banafjäl Bridge, but can be higher with other similar geometries.** The bridge's response is specially low because the critical wind speeds are moderate. Thus, small changes in geometry and natural frequencies can easily create greater effects.
- **Longer bridges with more than two beams might be very vulnerable to vortex shedding.** With more beams, section's height can remain equal even if the bridge is longer, having the same wind effects on a structure with a larger span.
- **For some cases, as with Banafjäl Bridge, an increase in the natural frequencies implies stronger vortex shedding actions.** Therefore, not always is better to increase stiffness.
- **Closing the section with wooden or steel plates is the best option to reduce vortex shedding effects.** It increases the critical velocity and reduces flow actions. However, this alternativve does not solve the problems in previous stages, as when only one beam is exposed to the wind.

6.2 Further research

The present study aimed to make a general description of wind effects and structure's response in this type of bridges. However, the complexity of the phenomenon requires a deeper research to reach more conclusive results. In order to do so, the following paths are proposed to continue the study of the problem:

- **Validation of results with wind tunnel tests.** As said in Section 1.4, CFD results can have considerable mismatches with the reality, specially when using simple turbulence models as the $k - \epsilon$ model. Therefore, is essential to run several wind-tunnel tests to validate the results.
- **Realisation of more simulations to study each relation in deep.** In this report only three different values were given to each geometrical parameter. Reducing the number of parameters it could be possible to evaluate better the relations detected in this report.
- **Design of empirical formulas to calculate each aerodynamic parameter.**
- **Introduction of the previous formulas in the analytical methods to check structure's limits.**
- **Realisation of more tests with three beams.** As said before, the number of beams allows to make slenderer bridges, which increases their vulnerability to dynamic effects.
- **Make more simulations with the concrete slab under construction.** When the concrete slab is not hardened yet, the bridge has all its mass but none of its stiffness, changing strongly its dynamic behaviour.
- **Test different types of bracing.** Changing the connections between the beams can modify the natural frequencies of the structure, changing its vulnerability to wind effects.

Bibliography

[1] Armit, J. In *Wind Structures. Lecture Series 89, Wind Effects on Buildings and Structures* (1976).

[2] Chen, J. M., and Fang, Y.-C. Strouhal numbers of inclined flat plates. *Journal of wind engineering and industrial aerodynamics 61*, 2-3 (1996), 99–112.

[3] Counihan, J. Adiabatic atmospheric boundary layers: a review and analysis of data from the period 1880–1972. *Atmospheric Environment (1967) 9*, 10 (1975), 871–905.

[4] Courtney, M., and Troen, I. Wind speed spectrum from one year of continuous 8 hz measurements. In *9. Symposium on turbulence and diffusion* (United States, 1990), N. Jensen, L. Kristensen, and S. Larsen, Eds., American Meteorological Society, pp. 301–304.

[5] Davenport, A. The prediction of the response of structures to gusty wind. *Safety of structures under dynamic loading 1* (1977), 257–284.

[6] Davenport, A. G. The application of statistical concepts to the wind loading of structures. *Proceedings of the Institution of Civil Engineers 19*, 4 (1961), 449–472.

[7] Davenport, A. G. The response of slender, line-like structures to a gusty wind. *Proceedings of the Institution of Civil Engineers 23*, 3 (1962), 389–408.

[8] Davenport, A. G. Gust loading factors. *Journal of the Structural Division 93*, 3 (1967), 11–34.

[9] Davenport, A. G. How can we simplify and generalize wind loads? *Journal of Wind Engineering and Industrial Aerodynamics 54* (1995), 657–669.

[10] De Sampaio, P., Coutinho, A. L. G. d. A., et al. Simulating vortex shedding at high reynolds numbers. In *The Tenth International Offshore and Polar Engineering Conference* (2000), International Society of Offshore and Polar Engineers.

[11] Deaves, D., and Harris, R. The structure of strong winds. In *Proc. CIRIA Conf. on Wind engineering in the eighties* (1980).

[12] Dyrbye, C., and Hansen, S. O. *Wind loads on structures*. 1997.

[13] ESDU 85020. Characteristics of atmospheric turbulence near the ground. part ii: single pont data for strong winds (neutral atmosphere).

[14] Eurocode 1. *Actions on structures - Part 1-4: General actions - Wind actions*. 2005.

[15] Feng, C. *The measurement of vortex induced effects in flow past stationary and oscillating circular and d-section cylinders.* PhD thesis, University of British Columbia, 1968.

[16] Giosan, I., and Eng, P. Vortex shedding induced loads on free standing structures. *Structural Vortex Shedding Response Estimation Methodology and Finite Element Simulation 42* (2013).

[17] Hansen, S. O. Vortex-induced vibrations of structures. In *Structural engineers world congress* (2007), pp. 2–7.

[18] Harris, R. The nature of the wind. *The modern design of wind-sensitive structures, Construction Industry Research and Information Association, London* (1971).

[19] Hoerner, S. F. *Fluid-dynamic drag: theoretical, experimental and statistical information.* Hoerner Fluid Dynamics, 1992.

[20] Kaimal, J. C., Wyngaard, J., Izumi, Y., and Coté, O. Spectral characteristics of surface-layer turbulence. *Quarterly Journal of the Royal Meteorological Society 98*, 417 (1972), 563–589.

[21] Kundu, P. K., Cohen, I. M., and Dowling, D. *Fluid Mechanics 4th.* Elsevier, 2008.

[22] Lam, K., and Wei, C. Numerical simulation of vortex shedding from an inclined flat plate. *Engineering Applications of computational fluid mechanics 4*, 4 (2010), 569–579.

[23] Laurence, D., and Mattei, J. Current state of computational bluff body aerodynamics. *Journal of Wind Engineering and Industrial Aerodynamics 49*, 1-3 (1993), 23–43.

[24] Liaw, K. *Simulation of flow around bluff bodies and bridge deck sections using CFD.* PhD thesis, University of Nottingham, 2005.

[25] Midway Alignment. The north bothnia line - good news and effects also for midway alignment.

[26] Mureithi, N. W., Xu, X., Baranyi, L., Nakamura, T., and Kaneko, S. Dynamics of the forced karman wake: Comparison of 2d and 3d models. In *ASME 2014 Pressure Vessels and Piping Conference* (2014), American Society of Mechanical Engineers, pp. V004T04A065–V004T04A065.

[27] National Building Code of Canada. *NBC 1990.* 1990.

[28] Petersen, E. L., Troen, I., and Frandsen, S. T. *Vindatlas for Danmark:(Beregning af vindmøllers energiproduktion. Vindmæssige forhold).* Forsøgsanlæg Risø, 1980.

[29] Radi, A., Thompson, M. C., Sheridan, J., and Hourigan, K. From the circular cylinder to the flat plate wake: the variation of strouhal number with reynolds number for elliptical cylinders. *Physics of Fluids 25*, 10 (2013), 101706.

[30] Roshko, A. On the drag and shedding frequency of two-dimensional bluff bodies.

[31] Ruscheweyh, H. Dynamische windwirkung an bauwerken. *Wiesbaden: Berlin, Bauverlag, 1982* (1982).

[32] Ruscheweyh, H. Further studies of wind-induced vibrations of grouped stacks. *Journal of Wind Engineering and Industrial Aerodynamics 11*, 1-3 (1983), 359–364.

[33] Ruscheweyh, H. Experience with the new european wind load code. *Journal of wind engineering and industrial aerodynamics 65*, 1-3 (1996), 243–260.

[34] Scanlan, R. The action of flexible bridges under wind, i: flutter theory. *Journal of Sound and Vibration 60*, 2 (1978), 187–199.

[35] Scanlan, R. The action of flexible bridges under wind, ii: Buffeting theory. *Journal of Sound and vibration 60*, 2 (1978), 201–211.

[36] Simiu, E. Wind spectra and dynamic alongwind response. *Journal of the structural division 100*, Proc. Paper 10815 (1974).

[37] Simiu, E. Revised procedure for estimating along-wind response. *Journal of the Structural Division 106*, 1 (1980), 1–10.

[38] Simiu, E., and Scanlan, R. H. *Wind effects on structures*. Wiley, 1978.

[39] Solari, G. Progress and prospects in gust-excited vibrations of structures. *Engng Mech 6* (1999), 301–322.

[40] Solari, G. The role of analytical methods for evaluating the wind-induced response of structures. *Journal of Wind Engineering and Industrial Aerodynamics 90*, 12-15 (2002), 1453–1477.

[41] Strømmen, E. *Theory of bridge aerodynamics*. Springer Science & Business Media, 2010.

[42] Strouhal, V. Über eine besondere art der tonerregung. *Annalen der Physik 241*, 10 (1878), 216–251.

[43] The Engineering Mindset. Properties of air at atmospheric pressure.

[44] Tu, J., Yeoh, G. H., and Liu, C. *Computational fluid dynamics: a practical approach*. Butterworth-Heinemann, 2018.

[45] Van der Hoven, I. Power spectrum of horizontal wind speed in the frequency range from 0.0007 to 900 cycles per hour. *Journal of meteorology 14*, 2 (1957), 160–164.

[46] Vickery, B. A model for the prediction of the response of chimneys to vortex shedding. In *Proc. 3rd Int. Symp. Design of Ind. Chimneys* (1978), pp. 157–162.

[47] Vickery, B. J., and Basu, R. I. Across-wind vibrations of structures of circular cross-section. part i. development of a mathematical model for two-dimensional conditions. *Journal of Wind Engineering and Industrial Aerodynamics 12*, 1 (1983), 49–73.

[48] Vickery, B. J., and Basu, R. I. Across-wind vibrations of structures of circular cross-section. part ii. development of a mathematical model for full-scale application. *Journal of Wind Engineering and Industrial Aerodynamics 12*, 1 (1983), 75–97.

[49] Vickery, B. J., and Basu, R. I. Simplified approaches to the evaluation of the across-wind response of chimneys. *Journal of Wind Engineering and Industrial Aerodynamics 14*, 1-3 (1983), 153–166.

[50] Vickery, B. J., and Clark, A. W. Lift or across-wind response to tapered stacks. *Journal of the Structural Division 98*, 1 (1972), 1–20.

[51] Von Karman, T. Progress in the statistical theory of turbulence. *Proceedings of the National Academy of Sciences of the United States of America 34*, 11 (1948), 530.

[52] Yakhot, V., Orszag, S., Thangam, S., Gatski, T., and Speziale, C. Development of turbulence models for shear flows by a double expansion technique. *Physics of Fluids A: Fluid Dynamics 4*, 7 (1992), 1510–1520.